Scanning Electrochemical Microscopy Investigations of Monolayer-protected Gold Nanoparticles and *Shewanella oneidensis*

By

David A. Crisostomo

Dissertation
Submitted to the Faculty of the
Graduate School of Vanderbilt University
in partial fulfillment of the requirements
for the degree of

DOCTOR OF PHILOSOPHY
in

Chemistry
May 2016
Nashville, Tennessee

Approved:

David E. Cliffel, Ph.D.

G. Kane Jennings, Ph.D.

Janet E. Macdonald, Ph.D.

David W. Wright, Ph.D.

To you

ACKNOWLEDGEMENTS

Financial support for the research presented here was provided by the National Science Foundation through the TN-SCORE program (DMR 0907619 and EPS 10040083) and the Scialog Program of the Research Corporation for Science Advancement.

Thank you to my advisor, Dr. David Cliffel. The breadth and depth of your knowledge in the field of analytical and electrochemistry will never cease to be impressive to me and I am glad to have had you as my advisor. Thank you for all the opportunities you provided me, especially the ability to present my work at three Pittcon conferences.

Thank you to my committee; Dr. Janet Macdonald, Dr. Kane Jennings, and Dr. David Wright for challenging me at all my examinations and allowing me this opportunity to defend my thesis.

The three projects presented in this dissertation are based on the work started by previous graduate students from the Cliffel Lab: Dr. Brian Turner, Dr. Rachel Peterson, and Dr. Gongping Chen. Thank you for doing the foundational work that made this research possible. Thank you especially to Dr. Brian Turner and Dr. Gongping Chen for teaching me how to use the scanning electrochemical microscope, a machine with so many idiosyncrasies that I affectionately refer to it as “SECM-bag.” Thank you also to Dr. Juan Tuberquia for muddling through with me as we learned how to use the SECM. Thanks to Dr. C. Ruth McNees and Dr. Emilianne McCranie from the Bachman Research Group for helping culture bacteria and Dr. Sean Elliott and his Research Group from Boston University for providing the bacteria.

Thank you to all the current and past members of the Cliffel lab that I had the opportunity to work with, especially Dr. Brian Turner, Dr. Kellen Harkness, Dr. Matthew Casey,

Mandy Agrawal, Adam Ryan Travis, and Evan Gizzie. I'd also like to acknowledge my undergraduate student Jennifer Ruddock and wish her luck on her graduate work.

Thank you to the editors of my work, especially Adam Ryan Travis and Dr. Danielle Kimmel, who are always willing and eager (sometimes too eager) to help me make my writing less terrible.

Thank you to the internet, the cause of, and solution to, all my graduate school problems.

Thank you to the fellow founders of the Lieutenant Junior Grade Nicholas "Goose" Bradshaw Memorial House (Jeremy Beam, Dr. Robert "B-money" Boer, and Alex Raubach) for making it an awesome place to live and a great getaway from the rigors of graduate school. Thank you also for letting me mooch at the house before this one, the Theodore Donald Kerabatsos Memorial House.

Thank you to my family. To my parents, Arthur and Nilda Crisostomo, whose constant support and encouragement made this possible. To my sister, Marisa Crisostomo, I wish you luck and success on your current pursuit of a Ph. D and hope I can continue to help you as you have helped me. Thank you all for checking in on me, even when I don't always respond right away.

Finally, to Anna Bitting for helping shoulder the burden of achieving a Ph. D. Your support is the only reason I was able to finish this. Thank you.

TABLE OF CONTENTS

LIST OF TABLES

LIST OF FIGURES

CHAPTER I

INTRODUCTION AND BACKGROUND

With the increasing need for alternative fuel solutions, solar energy devices have become vital facets of energy research. Currently, the development of alternative energy devices progresses at a steady, incremental pace.[1] However, this gradual progress is not enough to mitigate the imminent energy crisis.[2,3] The increasing demand for energy is coupled with an increasing demand for clean water, known as the energy-water nexus.[4] Just as water is necessary for fuel production, hydroelectric power, and cooling, energy is necessary for the treatment and delivery of water.[5] In order to meet the energy and water demands of increasing populations, multiple avenues of research are currently being explored.[4] The research presented in this dissertation contains fundamental research into the development of solar cells and microbial fuel cells. Solar cells typically have much lower water requirements than other forms of energy and microbial fuel cells combine water treatment with energy production. To circumvent the use of inadequate silicon-based electronics, the field of nano- and molecular circuits provides promising alternatives. In order to fully realize this possibility, methodologies for the synthesis and characterization of nanostructures must be thoroughly developed.

For solar cells, the long term goal is the fabrication of a three-dimensional nanocircuit capable of highly-efficient conversion of solar energy into electrical energy. The two main components of this nanocircuit are photosystem proteins and nanoparticles (Figure 1.1). While other research in the Cliffel group is focused on the optimization and development of photosystem photovoltaics,[6,7] this dissertation will discuss the investigations into the electrochemical properties of gold nanoparticles and their functions in the nanocircuit as capacitors and switches.

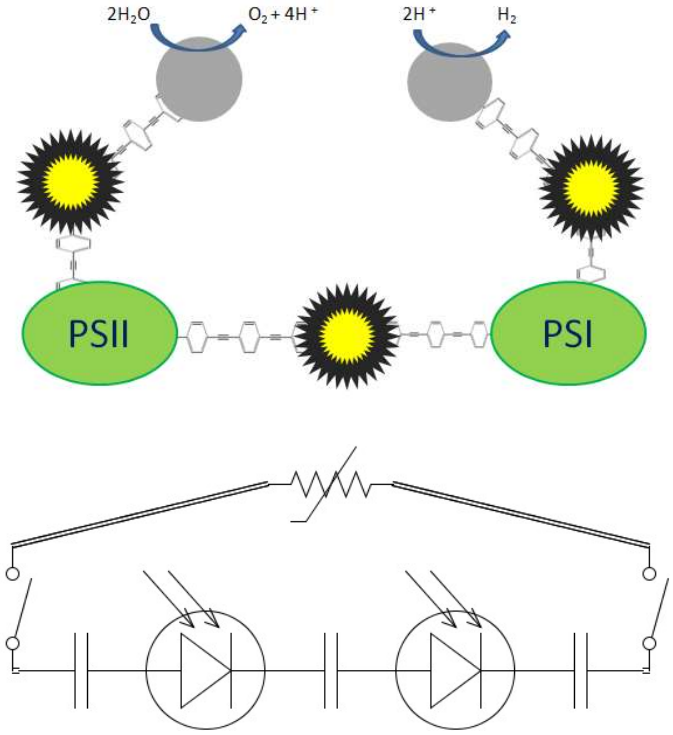

Figure 1.1. Diagram (top) showing a simplified design of combined nanotechnologies for splitting water as compared to convention circuit diagram (bottom). The reaction sites are PtNPs linked to monolayer-protected AuNPs acting as capacitors and switches. Photosystem I/II act as photodiodes, supplying electrons and holes to run the system.

Monolayer-protected Gold Nanoparticles

With unique and size-dependent electronic[8,9] and electrochemical[10,11] properties, monolayer-protected gold nanoparticles have been a research interest since their synthesis more than two decades ago.[12] Their unique structure (Figure 1.2) gives the monolayer-protected NP distinct advantages over other types of NPs like Au-citrate NP and quantum dots. The passivating layer makes the NP air stable and robust: capable of being dried and resuspended in solutions repeatedly without irreversible aggregation.[12,13] The protective ligand shell also determines the solubility of the AuNP. By using different thiolates as protecting ligands, both organic-soluble[14] and water-soluble[15] AuNPs can by synthesized.

A) B)

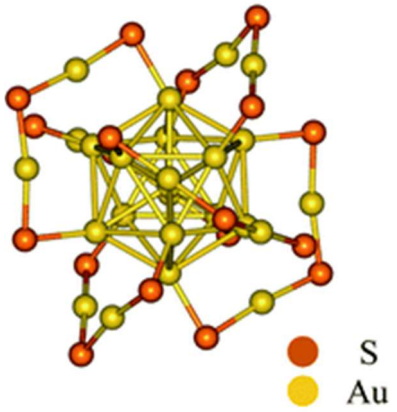

Figure 1.2. Simplified model of a monolayer-protected gold nanoparticle (A) versus the actual crystal structure (B) with "staple structures."[16]

One interesting property of monolayer-protected AuNPs is that the core-shell structure of the monolayer-protected AuNP causes the NP to act as a nanocapacitor.[17] The conductive gold core is electronically insulated from solution by the non-conductive ligands and creates a charge separation similar to a spherical capacitor. In Chapter III, we demonstrate the ability of these AuNPs to store multiple electrons and measure the electron transfer rate of the NPs using SECM.

Monolayer-protected AuNPs are also capable of being functionalized through place-exchange reactions. The place-exchange reaction requires a free ligand in solution to displace an attached protecting ligand (Figure 1.3).[13] As shown in Figure 1.2, the protective monolayer is actually a series of "staple structures" with gold-thiolate bonds located outside the core.[16,18] The place-exchange reaction is associative, requiring the free ligand to be simultaneously attached to the nanoparticle in an S_N2-like manner[19,20] and the staple structures facilitate this mechanism. In

Chapter III, the changes in electron transfer rate after functionalizing a variety of alkanethiolate-protected NPs with wire molecules using place-exchange are explored.

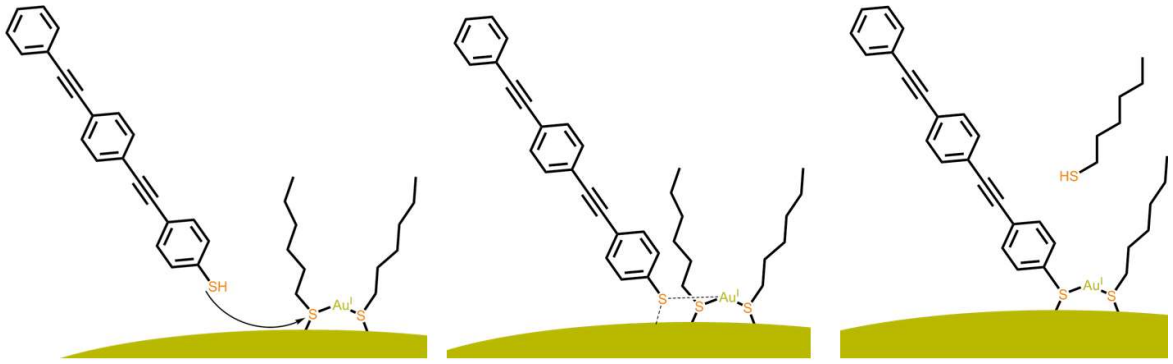

Figure 1.3. Associative mechanism as free thiol (B) displaces the protecting ligand (A) making a mixed monolayer NP and causing A to go into solution.

Chapter IV discusses the measurement of electron transfer rates of various water-soluble gold nanoparticles and demonstrates the effect of ligand charge. The NPs demonstrate pH-sensitive electron transfer rates and have the potential to be used as switches in the proposed nanocircuit.

Shewanella oneidensis

Shewanella oneidensis a bacteria species is named for the location it was first isolated from: sediments in Oneida Lake, NY in 1988.[21] After discovery that the bacteria were capable of reducing manganese (IV),[22] the various strains were denoted MR for "manganese reducing."[23] In this dissertation, *S. oneidensis* MR-1 is investigated. *S. oneidensis* is a species of gram-negative gammaproteobacteria with cellular dimensions of 2-3 μm in length and 0.4-0.7 μm in diameter.[24]

S. oneidensis has garnered attention for its ability to perform dissimilatory metal reduction (DMR), the process by which insoluble metals and substrates are reduced. DMR-capable bacteria, also known as exoelectrogens, are currently being studied for their role in bioremediation.[25] With

bacteria reducing toxic forms of heavy metals from ground water, these water sources can be restored to no longer pose a threat to human health.[26,27] In addition to *S. oneidensis* MR-1 capabilities to perform bioremediation, it has also been shown to generate electrical current in microbial fuel cells, making it a prime candidate for solving both sides of the energy-water nexus.[24]

While exoelectrogens are capable of directly transferring electrons into insoluble substrates using outer membrane proteins[28] and producing conductive protein nanowires,[29,30] *S. oneidensis* has been shown to predominately perform DMR with the production of soluble electron shuttles in the form of riboflavin.[31–33]

Understanding the capabilities and behavior of *S. oneidensis* MR-1 on electrodes is important in order to maximize its efficacy in bioremediation, microbial fuel cells, and electrosynthesis. In Chapter V of this dissertation, the DMR pathways of *S. Oneidensis* are explored. Using scanning electrochemical microscopy, we investigated the identification and electrochemical detection of soluble electron shuttles by *S. oneidensis* biofilms on electrodes, as well as spatially monitor the selective consumption and non-uniform production of the shuttle.

Scanning Electrochemical Microscopy

Scanning electrochemical microscopy (SECM) is a powerful electrochemical technique that links high-resolution spatial information to electrochemical experiments. By mounting a working electrode on a series of positional motors, the SECM is capable of providing information about the topography and spatial reactivity of a substrate as well as measure the electron transfer kinetics of analytes in solution. It is the primary technique used in the studies of this dissertation and the next chapter discusses SECM and its capabilities in-depth.

CHAPTER II

SCANNING ELECTROCHEMICAL MICROSCOPY

Introduction

One unifying component of this dissertation is the use of scanning electrochemical microscopy (SECM). This chapter will discuss the components and capabilities of SECM as well as the derivation of the equation used to find the electron transfer rates of gold nanoparticles.

Scanning Electrochemical Microscope

SECM utilizes a four electrode system (Figure 2.1). In addition to the reference and counter electrodes, there are two working electrodes: the tip and the substrate. The substrate electrode is typically a 2 mm diameter macroelectrode, inverted to create the bottom for the electrochemical cell. This electrochemical cell is mounted to a stationary stage. Above the stage, the tip electrode is mounted to two sets of positional motors: stepper motors and a piezoelectric positioner. The stepper motors have nominal positional resolution of 8 nm and a maximum translational distance of 50 mm. The piezoelectric positioner provides for finer x,y,z movement with a resolution of 1.6 nm.

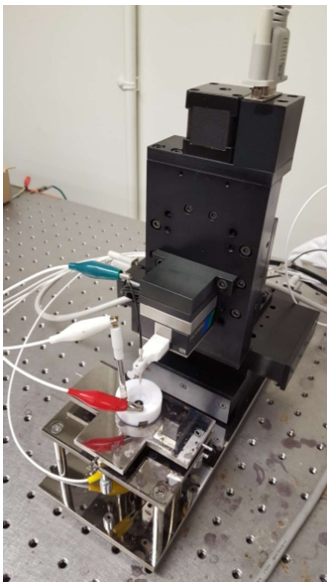

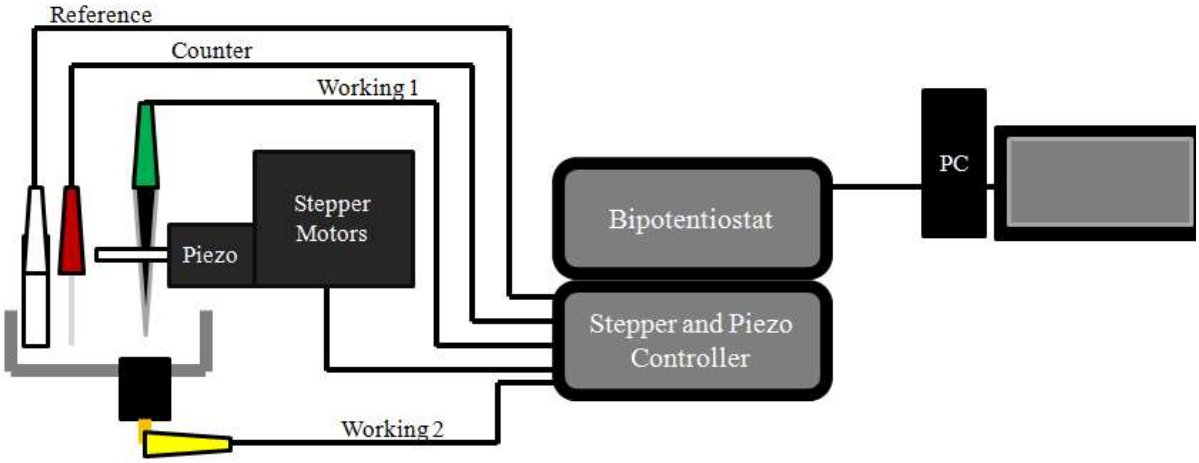

Figure 2.1. Picture of a scanning electrochemical microscope with corresponding block diagram.

The tip electrode is typically a disk ultramicroelectrode (UME) smaller than 25 μm in diameter. In bulk solution (Figure 2.2), the recorded current at the UME is mass-transfer limited and is dictated by Equation 2.1. Where n is the number of electrons transferred, F is the Faraday

constant, D is the diffusion coefficient, C* is the concentration of the analyte, a is the radius of the electrode.[34]

$$i_{t,\infty} = 4nFDC^{*}a \tag{2.1.}$$

However, once a tip electrode is moved in close proximity to a substrate the signal recorded at the tip is perturbed by a variety of factors including the thickness of the insulating glass on the UME, the conductivity of the substrate, and the distance of the tip from the substrate. This current-distance relationship can be exploited to extract electrochemical properties of both the analyte solution and the substrate.[34] Three main SECM techniques are applied in this dissertation: approach curves, substrate generation/tip collection, and imaging.

A) B)

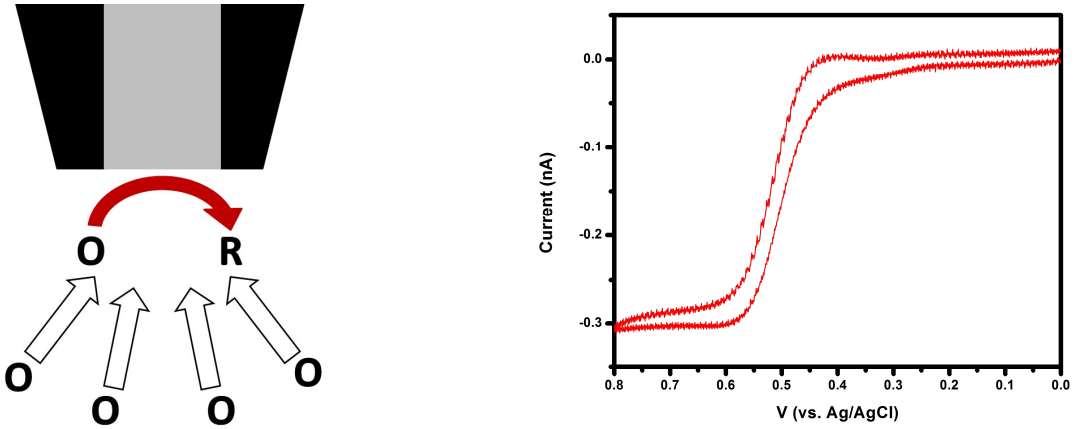

Figure 2.2. A) Illustration of a UME in bulk solution governed by hemispherical diffusion. B) Example of measured current from a UME.

Approach Curves

Approach curves, also known as feedback mode, are an SECM measurement used to interrogate electron transfer kinetics of an electroactive species. An approach curve is obtained by

measuring current at the tip electrode while moving it closer to the substrate. As the tip moves closer to the substrate electrode, the current is perturbed. As shown in Figure 2.3 (A), if the tip electrode is at a reducing potential and is approaching an insulating substrate, the current will decrease, and this results in negative feedback. This is due to the proximity of the substrate electrode hindering the flux of oxidized form (O species) from reaching the tip. However, if the substrate is a conductive material, the reduced form (R species) produced during the reaction can diffuse to the substrate and be regenerated as O species. This regeneration of O species results in an increase in current or positive feedback. The rate at which this positive feedback occurs gives information as to mass-transfer limited and kinetically limited electron transfer rates of an analyte.

A)

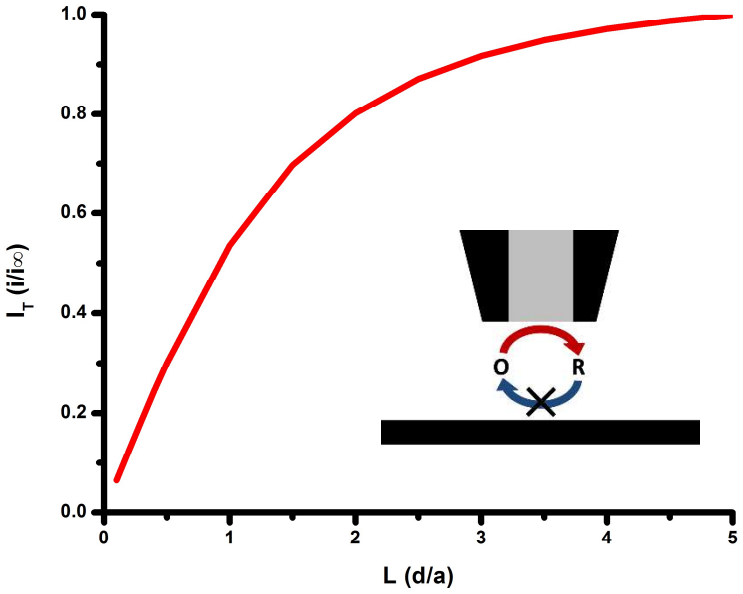

B)

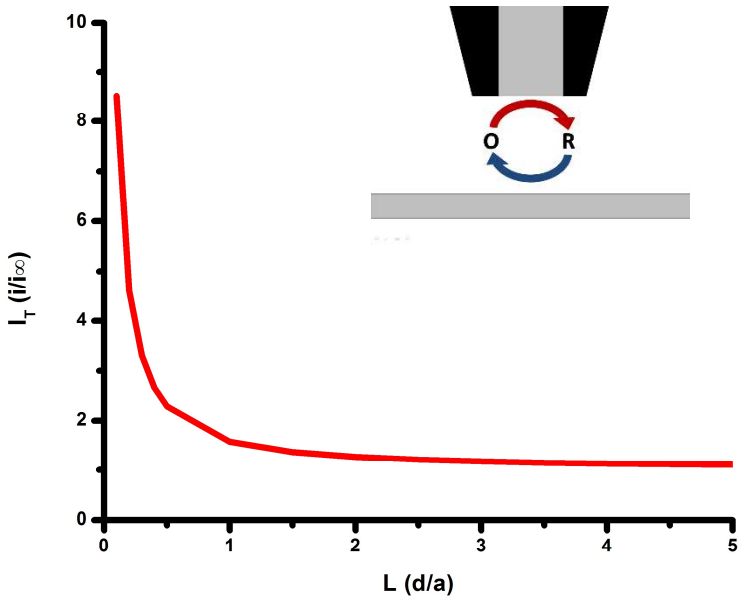

Figure 2.3. Theoretical approach curves demonstrating the effect on current of a UME tip electrode as it approaches an insulating substrate (A) and conductive substrate (B).

Analyzing Approach Curves

In attempts to create a simpler means of analyzing SECM data, Dr. Rachel Peterson derived an equation in her dissertation where the only unknown variable was the forward heterogeneous reaction rate of the SECM system, otherwise known as the electron transfer rate.[14]

The electron transfer rate of an analyte is determined by both mass-transfer limited and kinetically limited processes. In order to determine the rates of these processes, the system design must have one limit dominating the other. In the case of SECM, the size of the tip electrode determines whether the system will be mass transfer limited or kinetically limited. The observed current for mass transfer limited process (i_l) follows

$$i_l = nFAm_oC^* \tag{2.2.}$$

where n is number electrons transferred, A is the area of the electrode, m_o is the mass-transfer coefficient of the analyte, and C^* is the bulk concentration of the analyte.[35] In SECM feedback mode, an approach curve is recorded. When the tip is far from the substrate (>7 tip diameters), the current is limited by steady state diffusion. The mass transfer coefficient for steady state diffusion to a UME is

$$m_{t,\infty} = \frac{4D}{\pi a} \tag{2.3.}$$

where D is the diffusion coefficient and a is the radius of the UME. Substituting $m_{t,\infty}$ for m_o gives the equation for steady state current as defined by Equation 2.1

For analysis of an SECM approach curve, the measured current i_l is normalized by dividing i_l by $i_{t,\infty}$, which leaves the dimensionless current parameter I_T. To evaluate the limiting factor in the approach curve current, I_T is plotted against the dimensionless distance parameter L (where L=d/a, where d is the distance separating the UME from the substrate) resulting in

$$I_T(L) = \frac{i_l}{i_{t,\infty}} = \frac{Am_o}{4Da} = \frac{\pi a m_o}{4D} \quad (2.4.)$$

showing that I_T is independent of solution concentration and number of electrons transferred.[36–38] The mass transfer coefficient can be determined by solving the above equation for m_o, resulting in

$$m_o = I_T\left(\frac{4D}{\pi a}\right) \quad (2.5.)$$

Upon substituting Equation (2.3) into the above equation, it is shown that the mass transfer coefficient dependent on L is described as

$$m_o = I_T m_{t,\infty} \quad (2.6.)$$

In equation (2.5), it is shown that the mass transfer coefficient is inversely proportional to the radius of the tip electrode used. Therefore, with smaller tip sizes, the system is less affected by mass transfer processes.[36,38] A theoretical model of mass-transfer limited current for positive feedback was computationally determined[38] to be

Any negative deviations from the above equations indicate a kinetically limited system.

$$I_T = 0.68 + \left(\frac{0.78377}{L}\right) + 0.3315e^{\left(-\frac{1.0672}{L}\right)} \quad (2.7.)$$

In order to determine the electron-transfer kinetics of a system, the tip electrode must be small enough in diamter to mitigate any mass-transfer limitations.[37,38] The current for kinetically limited processes is described as

$$i_k = nFAk_f C^* \quad (2.8.)$$

where k_f is the electron transfer rate.[36] Because experimental electron transfer rate is a combination of mass-transfer and kinetic-transfer, the current can be modeled as parallel resistors in a circuit[35,39]

$$\frac{1}{i_{exp}} = \frac{1}{i_l} + \frac{1}{i_k} \quad (2.9.)$$

which can be translated to

$$i_{exp} = \frac{i_l i_k}{i_l + i_k} \tag{2.10.}$$

Substituting Equation (2.2) and Equation (2.8) into the above relationship results in

$$i_{\exp} = nFA\left(\frac{mk_f}{m + k_f}\right)C^* \tag{2.11.}$$

In order to analyze the kinetic component, the steady state current must also be written as parallel resistors. Combining equations (2.2) and (2.1) into equation (2.10.) results in

$$i_{t,\infty} = nFA\left(\frac{m_{t,\infty}k_f}{m_{t,\infty} + k_f}\right)C^* \tag{2.12.}$$

To obtain the dimensionless experimental current parameter I_T, $i_{(exp)}$ is divided by $i_{t,\infty}$ to give

$$I_{T,mix} = \frac{i_{\exp}}{i_{t,\infty}} = \frac{\left(\frac{mk_f}{m + k_f}\right)}{\left(\frac{m_{t,\infty}k_f}{m_{t,\infty} + k_f}\right)} \tag{2.13.}$$

Simplified to

$$I_{T,mix} = \frac{(I_T(m_{t,\infty} + k_f))}{(I_T m_{t,\infty} + k_f)} \tag{2.14.}$$

Substitution of equation (2.3.) results in

$$I_{T,mix} = \frac{I_T(\frac{4D}{\pi a} + k_f)}{\frac{4D}{\pi a}I_T + k_f} \tag{2.15.}$$

In which, after substituting $I_T(L)$

$$I_{T,mix} = \frac{\left(0.68 + \left(\frac{0.78377}{L}\right) + 0.3315e^{\left(-\frac{1.0672}{L}\right)}\right)\left(\frac{4D}{\pi a} + k_f\right)}{\frac{4D}{\pi a}\left(0.68 + \left(\frac{0.78377}{L}\right) + 0.3315e^{\left(-\frac{1.0672}{L}\right)}\right) + k_f} \qquad (2.16.)$$

is an equation in which there is only one unknown variable: k_f, the forward heterogeneous rate constant or electron transfer rate. In order to analyze this value, $I_{(T,mix)}$ was fit to experimental approach curves by varying k_f using the least-squares method (appendix A).

This form of analysis of electron transfer rate has a number of advantages. First, it does not require the use of complex multiphysics analysis programs like COMSOL or FEMLAB, which require development of models and equations to accurately model a system. Other non-computational methods and equations for determining electron transfer require information which is typically indeterminate for monolayer-protected nanoparticles (MPNs): standard redox potential, number of electrons transferred, and concentration. Standard redox potential cannot be determined unless a sample exhibits quantized double-layer (QDL) charging peaks. The number of electrons transferred can also be determined by QDL peaks, but in the absence of peaks, the number cannot be determined. Concentration of NPs can be estimated using a combination of transmission electron microscopy (TEM) and thermogravimetric analysis (TGA) but cannot be determined exactly. Since equation (2.16) relies on only knowing the diffusion coefficient of the analyte and the radius of the tip electrode, it eliminates the need for the above information, making it an easier and more accurate analysis.

Substrate Generation/Tip Collection

Generation/collection experiments offer spatial electrochemical information about a substrate by measuring the current collected at the tip electrode positioned above a substrate (Figure 2.4). The method used in this dissertation was substrate generation/tip collection (SG/TC).

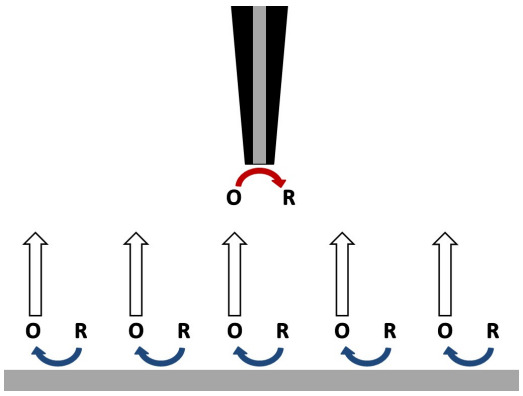

Figure 2.4. Substrate generation-tip collection mode of SECM where the substrate generates the O species which diffuses to the tip electrode to be reduced and measured as current.

The substrate electrode is much larger than the tip electrode and creates a large diffusion layer of analyte. The tip electrode is able to record reduction currents without perturbing this diffusion layer due to its small electroactive area relative to the substrate area.

Using a similar system to SG/TC, an SECM image can be obtained by rastering the tip across a substrate in the x-y plane and monitoring the tip current as a function of tip location in "constant height mode."[34] Shown in Figure 2.5, measuring the current on the tip electrode as it passes over a surface allows the mapping of either conductivity of featureless surfaces (direct current output) or topography (with a corresponding current vs. height calibration curve).

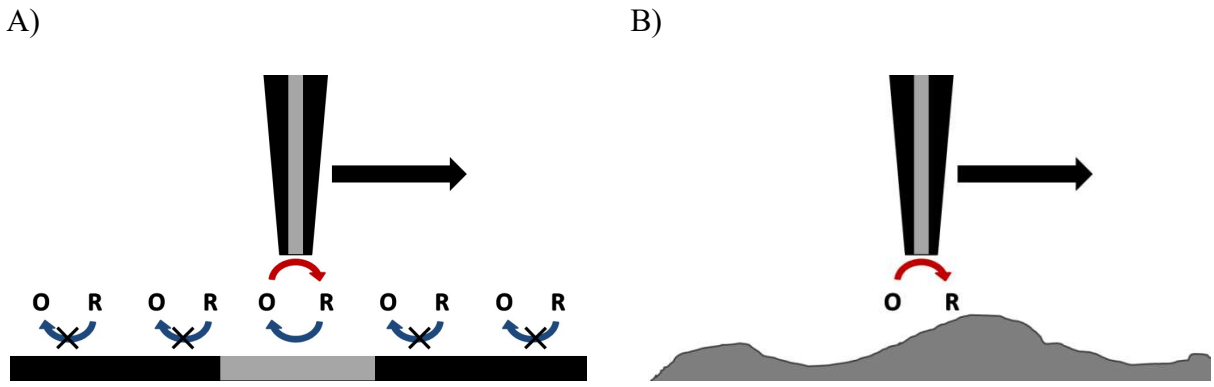

Figure 2.5. SECM imaging of a substrate with varying surface (A) reactivity and (B) topography.

One unique ability for SECM imaging is reaction rate imaging.[34,40] By positioning the tip electrode above a reactive surface, current on the tip can be used to measure the diffusion profile of an individual reaction site as it produces analyte that diffuses towards the tip. Using this technique, the spatial relationships of the chemical and electrochemical reactivity have been investigated on a variety of substrates including porous membranes,[41,42] polymers,[43] and films.[44] SECM imaging has also been conducted on biological systems including bacteria and biofilms and has been used to quantify and spatially resolve metabolite production in real-time.[45–47]

Using these SECM imaging techniques, we are capable of investigating *S. oneidensis* biofilms to elucidate its dissimilar metal reduction (DMR) mechanism by providing spatially resolved measurements in real-time.

CHAPTER III

MODULATING ELECTRON TRANFER RATE IN MONOLAYER-PROTECTED GOLD NANOPARTICLES WITH MOLECULAR WIRES

Introduction

Before incorporating nanoparticles into molecular circuits and utilizing their electrochemical properties, nanomaterial electron transfer properties must be fully understood. Previous work has shown that the composition of the protecting monolayer can impact the electron transfer rates of gold nanoparticles (AuNPs).[14] Both the length and structure of the monolayer have been shown to affect electron transfer on two-dimensional self-assembled monolayers (SAMs) on gold electrodes.[48,49] With gold nanoparticles acting as three-dimensional SAMs,[13] we hypothesize that addition of more conductive ligands into a AuNP protecting monolayer will increase electron transfer.

Electrochemical Properties of Gold Nanoparticles

Gold nanoparticles are versatile due to their size-dependent electrochemical properties including charging,[50] electron transfer,[10] and film conductivity.[11] Charging of NPs occurs much like a standard metal electrode, making it ideal for use in nanocircuits.[35] As electrons are added or removed from the surface of the particle, supporting electrolyte charges attempt to adsorb onto the surface to balance the charge, which results in charge separation. AuNPs have three classes of charging: bulk, quantized, and molecule-like.[51]

Gold NPs greater than 3-4 nm in diameter exhibit bulk properties governed by

$$\Delta V = \frac{ze}{C_{CLU}} \tag{3.1}$$

where ΔV is the change of electrochemical potential of a NP with a double layer capacitance of C_{CLU} resulting from the movement of z electrons in and out of the particle. Cyclic voltammograms of "bulk" sized metal NPs are largely featureless but current slowly rises with increasingly negative potentials.[52]

At less than 3 nm in diameter, AuNPs act as nanocapacitors capable of going through multiple redox states. These multiple redox states occur through a sweeping voltage as electrons move in and out of the particle creating the phenomenon known as quantized double layer capacitance (QDL).[17] QDL charging occurs because the length of the ligands creates a thick enough monolayer, relative to the size of the particle, to create a large charge separation. A charge separation across a non-conducting material is a capacitor. As such, capacitance of quantized sized NPs (C_{NP}) is governed by

$$C_{NP} = A_{NP}\left(\frac{\varepsilon\varepsilon^{o}}{r}\right)\left(\frac{r+d}{d}\right) = 4\pi\varepsilon\varepsilon^{o}\left(\frac{r}{d}\right)(r+d) \qquad (3.2)$$

Where A_{NP} is the surface area, ε is the effective dielectric constant of the monolayer, ε^{o} is permittivity of free space, r is the radius of the particle, and d is the thickness of the monolayer.[51]

As shown in the above equation, both the size of the particle and the thickness of the monolayer affect the capacitance of the particle, thus impacting which potentials the particle will be charged and discharged.[2] In the case of monodisperse particles, with a narrow particle size distribution, charging and discharging occurs simultaneously, leading to the observation of multiple reversible redox peaks in cyclic voltammetry (Figure 3.1). In order to remove the influence of non-faradaic current, square wave voltammetry was used (Appendix A). Shown in Figure 3.2, these particular C_6-AuNPs are capable of storing and reversibly discharging 7 electrons.

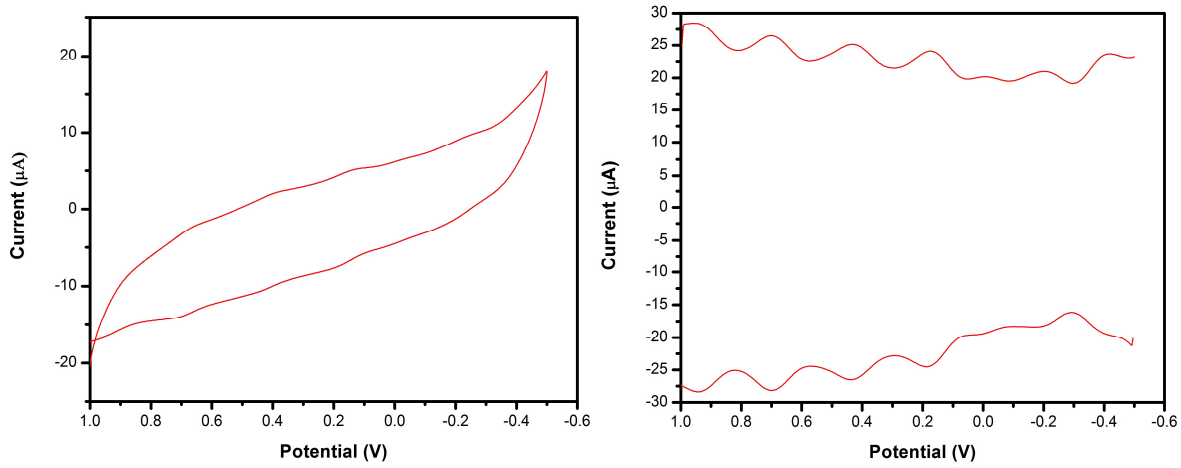

Figure 3.1. CV (left) of monodisperse C_6-AuNPs demonstrating multiple charging and discharging peaks compared to SWV (right) of monodisperse C_6-AuNPs with clearly defined peaks.

If polydisperse, however, the particles will charge and discharge at various potentials, causing the peaks to overlap in a kind of destructive interference resulting in a featureless curve. Furthermore, Hicks et. al. demonstrated that by increasing the thickness of the protecting monolayer by using longer alkane chain thiols, the relative intensity of the charging peaks decreases, indicative of slower electron transfer rates.[50]

Wire Molecules

In order to create molecular electronics, there must be the ability to synthesize and utilize molecular wires to connect the different components to one another. Molecular wires typically have delocalized highest occupied molecular orbitals (HOMO) that are close to the Fermi level of a metal (Figure 3.2).[53] When a wire molecule is attached to a metal electrode, electrons are capable of flowing through the molecule through the inner-sphere tunneling mechanism "resonant tunneling."[54]

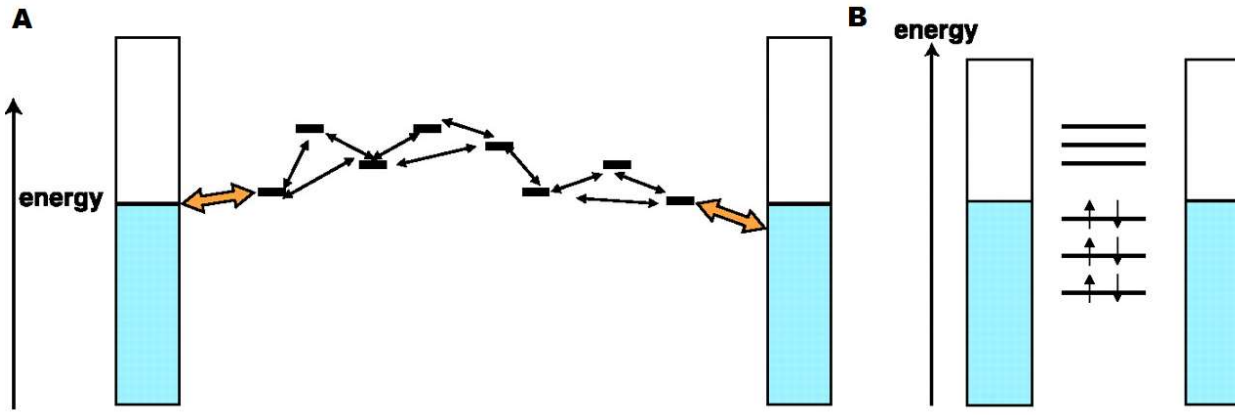

Figure 3.2. (A) Schematic of the multiple electron sites of a molecular wire with black arrows representing intersite interactions along the molecule with gold arrows showing the energy coupling with the electrode. (D) is the molecular orbital diagram of the same system, demonstrating the Fermi level of the electrode within the HOMO-LUMO gap.[53]

This type of tunneling can occur in aromatic structures with high levels of π-conjugation due to their rigid and planar structures.[55] This conjugation causes the molecular orbital to extend across the entire molecule as a single electron cloud similar to a metal. Because of these requirements, most research into molecular wires has been done on conjugated oligomers.[56–60]

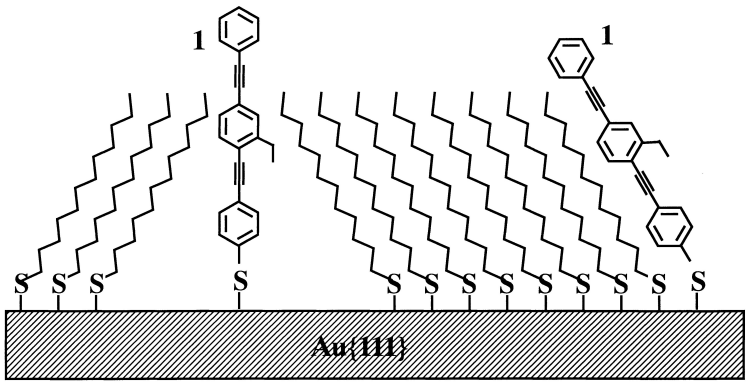

Figure 3.3. Schematic representation of the Au-bound molecular wire candidate wire molecule in two possible orientations after insertion into a dodecanethiolate film.[61]

In one early study, scanning tunneling microscopy (STM) was used to measure the conductivity of single molecular wires.[61,62] Shown in Figure 3.3, this molecule was added to a self-assembled monolayer of dodecanethiol on gold. As shown below in Figure 3.4, bright isolated spots appeared at defect sites on the SAM. By measuring the changes in current as the STM tip is moved in the Z direction, it was found that the relative apparent tunneling-barrier height (ATBH) of the molecular wires compared to the rest of the SAM was at least two times lower.

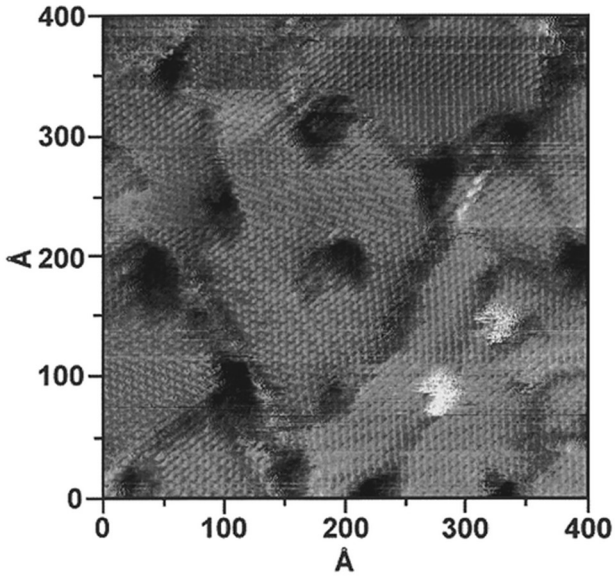

Figure 3.4. A constant current STM topography of a dodecanethiolate monolayer on gold with inserted wire molecules. The wire molecules appear as peaks in topography (displayed as bright). They insert at structural domain boundaries in terraces of dodecanethiolate SAM.[61]

More recently, experiments have been conducted to enhance the electron transfer properties of molecular wires.[60] In this study, the conductivity of two types of molecular wires were studied. Carbon-bridged oligo-p-phenylenevinylene (COPV) was compared to an equivalent flexible molecular bridge (Figure 3.5.).

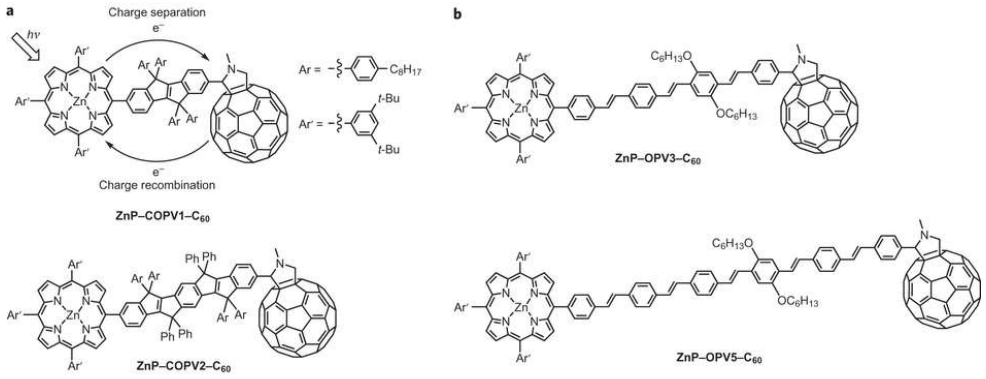

Figure 3.5. Carbon-bridged oligo-p-phenylenevinylene (a) versus flexible counterparts (b).[60]

It was determined that rigid, fully planar molecular wires only transfer electrons through tunneling as opposed to electron hopping. The COPV type molecular wire had electron transfer rates 840 times faster than its comparable flexible form. Only 140 of this factor is due to increased conjugation so the remaining enhancement is due to inelastic electron tunneling.

In order to minimize the potential for electron hopping and ensure the ability of the wire to use the resonant tunneling mechanism, S-[4-(2-phenylethynyl)phenyl]ethynylphenyl]thiol or PEPEPSH (Figure 3.6) was chosen. Fully conjugated and rigid, this molecule is an ideal molecular wire. Previous work has shown that these molecular wires have conductivies at least an order of magnitude over alkanethiolate chains of comparable length.[63] By forming SAMS with a variety of alkane and alkyl thiolate chains on separate metal junctions and slowly bringing them in contact with each other, the conductivity of the SAM could be measured.

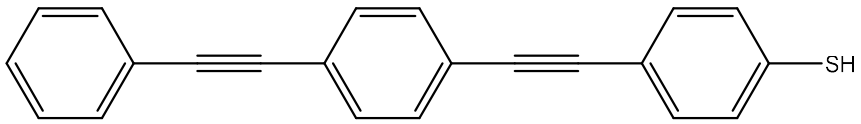

Figure 3.6. S-[4-(2-Phenylethynyl)phenyl]ethynylphenyl]thiol

Results and Discussion

As discussed in Chapter II, the SECM approach curves are graphed as normalized current (I_T) vs. distance L (d/a). The equation 2.15 is then fit to the experimental data to determine the electron transfer kinetics for the AuNPs.

In Figure 3.7, the unwired dodecanethiolate protected gold nanoparticles (C_{12}-AuNPs) exhibit slow electron transfer rates (0.0015±0.0003 cm/s). Upon place exchange of PEPEPSH, the k_f more than doubled (0.0039±0.0008 cm/s). This is in agreement with previous studies

demonstrating increased electron transfer rates with more conductive protecting ligands.[9] This trend is continued with the k_f of unwired octanethiolate protected gold nanoparticles (C_8-AuNPs) of 0.003±0.001 cm/s increasing to 0.008±0.002 cm/s with a similar addition of PEPEPSH (Figure 3.8)

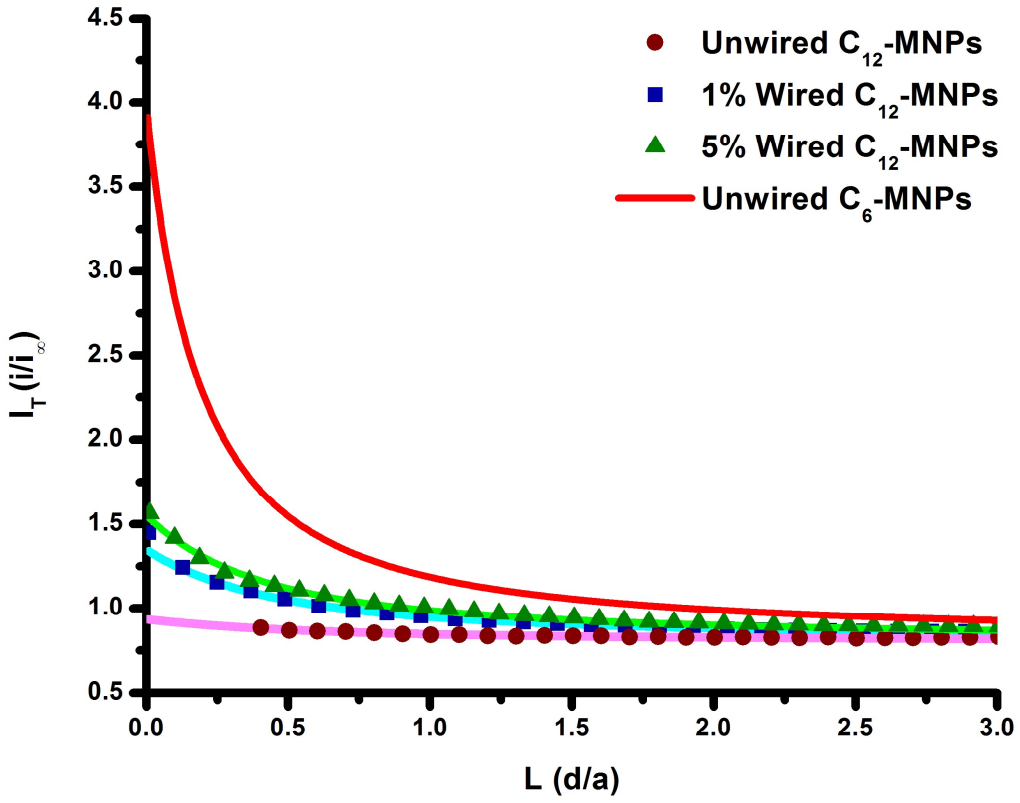

Figure 3.7. Approach curve fits for C_{12}-AuNPs with various wire concentrations showing decreasing k_f with an increasing number of wire molecules in the monolayer. The tip electrode was held at 0.6 V and the substrate electrode at 0 V (vs. Ag/Ag^+ pseudo-reference).

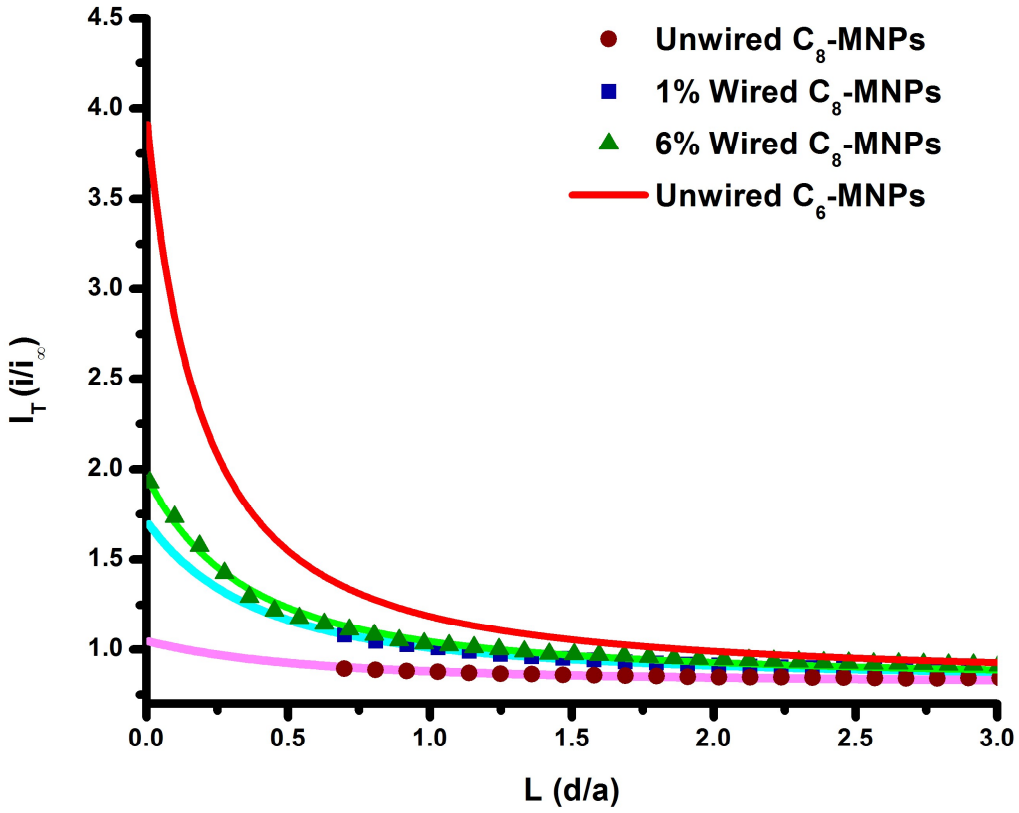

Figure 3.8. Approach curve fits for C_8-AuNPs with various wire concentrations showing increasing k_f with an increasing number of wire molecules in the monolayer. The tip electrode was held at 0.6 V and the substrate electrode at 0 V (vs. Ag/Ag^+ pseudo-reference).

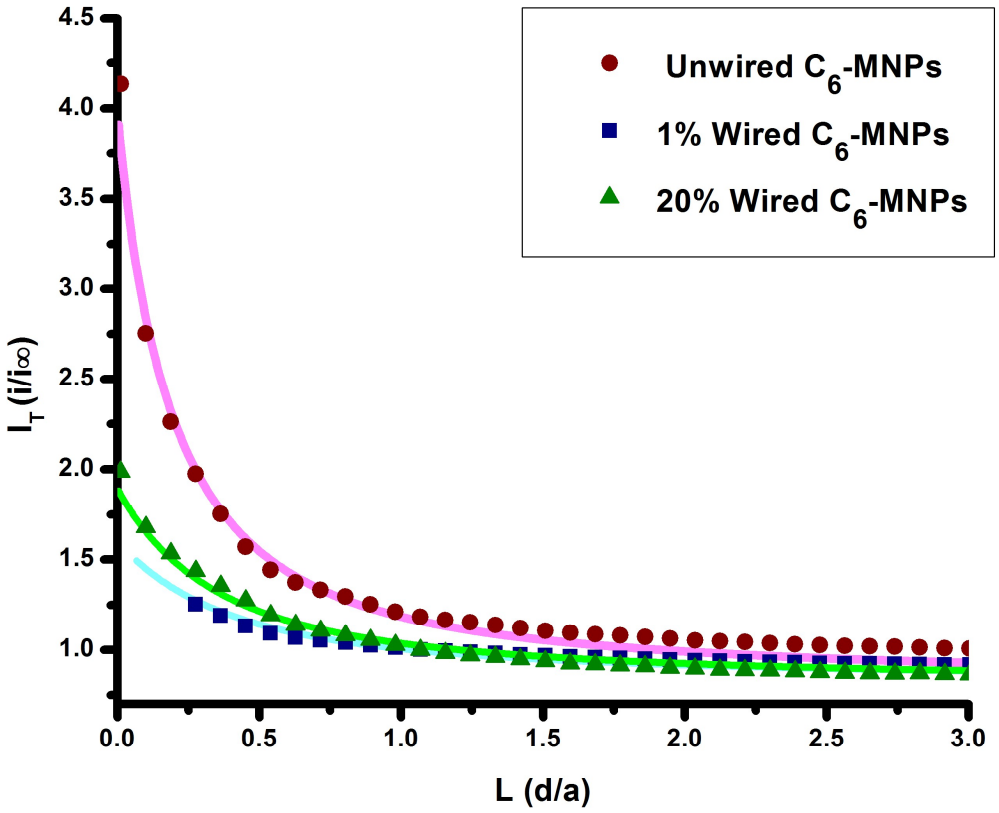

Figure 3.9. Approach curve fits for C_6-AuNPs with various wire concentrations showing decreasing k_f with an increasing number of wire molecules in the monolayer. The tip electrode was held at 0.6 V and the substrate electrode at 0 V (vs. Ag/Ag^+ pseudo-reference).

With these findings, it was hypothesized that electron transfer rate of C_6-AuNPs could be increased with a similar addition of PEPEPSH. However, after a small addition of wire (around 1%) it was found that there was no statistical difference between the electron transfer rates of unwired C_6-AuNPs (0.010±0.004 cm/s) and 1% wired C_6-AuNPs (0.008±0.001 cm/s) (Figure 3.9). After place exchanging a greater amount PEPEPSH (approximately 3%), the electron transfer rate was reduced more than an order of magnitude (0.0006±0.0003 cm/s).

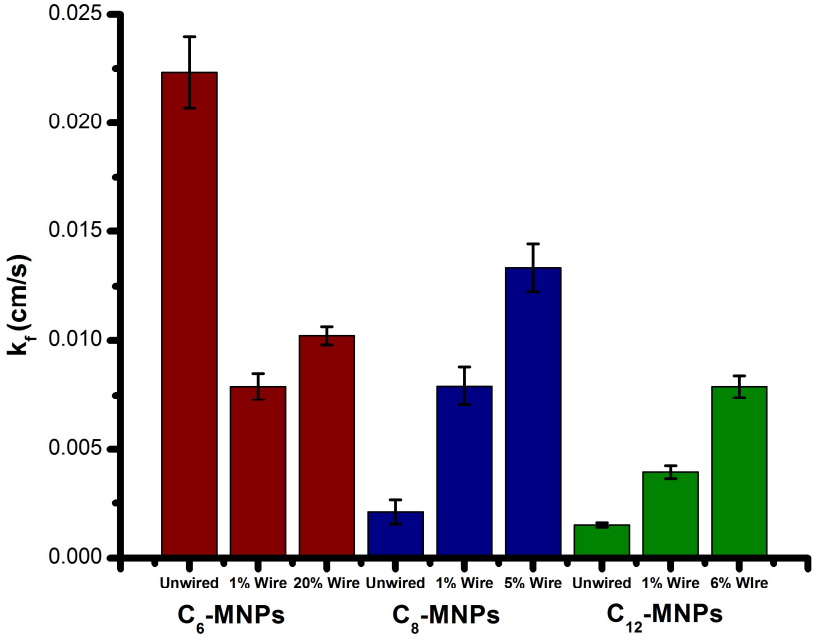

Figure 3.10. Electron transfer rates (k_f) of both wired and unwired C_6-, C_8-, C_{12}-AuNPs showing increasing k_f for C_{12}-AuNPs and C_8-AuNPs but decreasing k_f for C_6-AuNPs. Standard error associated with multiple measurements (n>8).

This evidence confirms that the electron transfer kinetics of the wire molecule (inner-sphere resonant tunneling) is fundamentally different from the kinetics of typical nanoparticle electron transfer (outer-sphere through-space tunneling). It was hypothesized that resonant tunneling would always be faster than the through-space mechanism and while this is the case for

C_8- and C_{12}-AuNPs, the reverse is true for C_6-AuNPs. (Figure 3.10) This contradiction can be explained by the relative lengths of the different protecting ligands.

The length of dodecanethiol is comparable to the length of the wire molecule; and, while shorter, octanethiol is still more than half the length of PEPEPSH. In contrast, hexanethiol is considerably shorter than the wire. As discussed above, electron transfer rate is slowed with increased monolayer thickness. Resonant tunneling is also length dependent.[55] Because octanethiol and dodecanethiol are more similar in length to PEPEPSH, the electron transfer rate is increased due to resonant tunneling being faster at that length. The difference between hexanethiol and PEPEPSH is so large, however, that the length of the wire molecule becomes the dominant factor. Furthermore, because PEPEPSH is a rigid structure, it also prevents shorter chain protecting ligands from reducing the tunneling distance by being in close proximity with the electrode. This increased average distance further inhibits electron transfer (Figure 3.11).

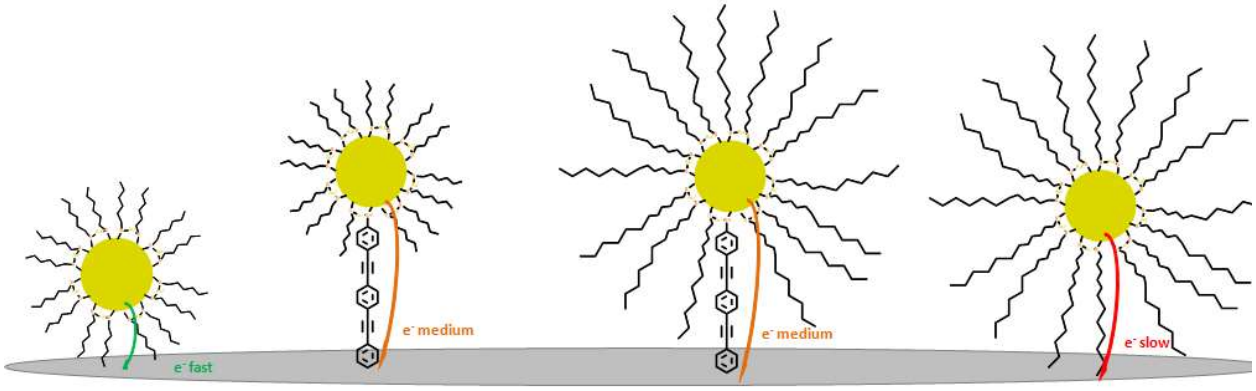

Figure 3.11. While the highly conductive molecular wire is capable of increasing the electron transfer rate of longer protecting ligands (right), the rigid structure increases the tunneling distance for shorter ligands (left) and slows electron transfer instead.

The dramatic effect on electron transfer rate from small additions of wire is evidence that the rotational speed of the nanoparticles is faster than the electron transfer. First, the large increase in k_f from a small addition of wire indicates that the effective conductivity of the entire monolayer has been altered. If the rotational speed of a nanoparticle were slower than electron transfer, the effect of 1% wire should have been much smaller as it would be much less likely that the shortest path for the electron to transfer would have been accessible through the wire on the electron transfer timescale. Second, there is a diminished effect with higher concentrations of wire on the MPN (Figure 3.10). This slight increase in electron transfer rate is not proportional to the increased concentration of wire, indicating that the rotational speed is fast enough that the likelihood of transferring through a wire molecule is not linearly increased by the presence of additional wire.

In summary, the kinetically limited heterogeneous electron transfer rate of wired and unwired MPNs was measured using scanning electrochemical microscopy. Although the wire molecule was shown to increase the k_f for both C_{12}-MPNs and C_8-MPNs, the additional length and rigidity of the wire caused a decrease in electron transfer rate for C_6-MPNs. Thus, it was shown that wire molecules can only be used to increase electron transfer rates for ligands of similar lengths. The fact that these rates increase with very small amounts of wire indicate that the rotational speed of a nanoparticle is much faster than the timescale of electron transfer.

Experimental

Nanoparticle Synthesis

Nanoparticles were synthesized using a modified Brust method.[12] 0.1 g of $HAuCl_4$ was transferred into 30 mL of toluene using 1.0 M tetraoctylammonium bromide. The organic layer

was separated and cooled to 0ºC and reacted with an alkanethiol (3:1, mol/mol) until colorless. Then, 10:1 mol/mol sodium borohydride in ~1 mL of 0ºC DI water was added and the mixture reacted for 3 h. The reaction was then concentrated to 10 mL using rotary evaporation and nanoparticles were precipitated out of ethanol overnight. The nanoparticles were cleaned using centrifugation and suspension in successive steps of ethanol, acetone, and acetonitrile and were characterized using ^{1}H-NMR and TEM.

Molecular Wire Deprotection

Two methods of deprotection were used. First, approximately 0.07 g of PEPEPSAc was dissolved in 4 ml of dichloromethane and 1 ml of methanol in a round bottom flask with a condenser. A few drops of concentrated sulfuric acid were then added to this solution. The flask was then purged with nitrogen and sealed, and the reaction was allowed to progress for 2 h before separation.

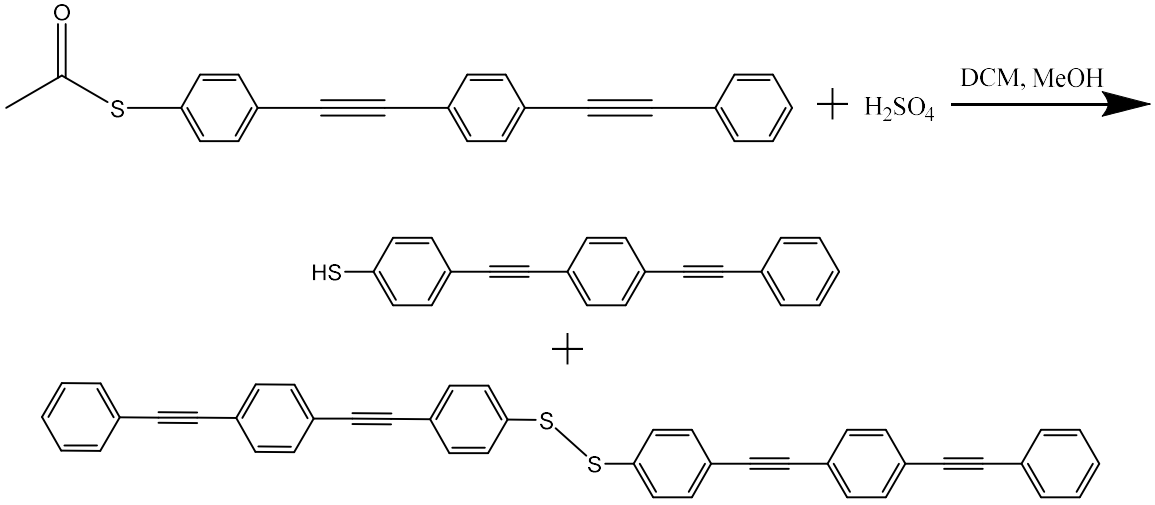

Scheme 3.1. Deprotection of PEPEPSAc to thiol and disulfide products.

As seen in the scheme above, the expected products for this reaction include both the thiol, S-[4-(2-Phenylethynyl)phenyl]ethynylphenyl]thiol (PEPEPSH) and the disulfide, di-S-[4-(2-Phenylethynyl)phenyl]ethynylphenyl]thiol, $(PEPEPS)_2$.

In order to separate these products, a column of silica gel in hexanes. The separation was done with an increasing gradient of DCM in hexanes (10% DCM to 100%). The first fractions collected yielded a white solid after vacuum evaporation of solvent whereas later fractions contained a yellow solid.

For the second deprotection method, 0.05 g of PEPEPSAc was dissolved in 5 ml of ethanol under nitrogen. Next, 0.06 g of NaOH in 10 ml of water was added dropwise. The reaction was then refluxed for 2 h. After cooling to room temperature, the solution was neutralized using a 2M HCl solution. The solution was then transferred to a separatory funnel and extracted with diethyl ether. The organic layer was dried over Na_2SO_4, and solvent was removed using rotary evaporation.

The resulting yellow solid was dissolved in hexanes and then centrifuged. The precipitate from centrifugation was then collected and the solution was subject to rotary evaporation, leaving a solid. Both the hexane-soluble and hexane-insoluble portions were analyzed using ^{1}H-NMR in deuterated DCM. It was found that the hexane-insoluble portion was more pure, and this product was used for subsequent place exchange reactions.

A CH Instruments 920D Scanning Electrochemical Microscope was used to collect approach curves and voltammograms. The tip electrode was a 10 μm diameter Pt UME. A 2 mm Pt disk electrode was used as the substrate electrode. The counter electrode was a Pt wire. A silver wire treated with hydrochloric acid was used as a Ag/Ag^+ pseudo-reference. All measurements

were performed in anhydrous methylene chloride with $TBAPF_6$ supporting electrolyte (200 mM). AuNP concentration was approximately 5 mg/mL.

Wire molecules were added to AuNPs using place exchange. 1 mg of PEPEPSH was mixed with 5 mg of AuNPs in approximately 5 ml of toluene and stirred for at least 24 h. C_6-protected AuNPs required additional reaction time (up to 72 h). Place exchange rates were determined through ^{1}H-NMR and found to be around 1%.

Determination of Wire Concentration on AuNPs

Wire concentration was determined qualitatively using ^{1}H-NMR. By calibrating the integration of the peaks of the entire alkane chain (around 1-3 ppm) as 1 proton (Figure 3.10), the integration of the aromatic peaks (between 7-8 ppm) gives the percentage of ligands on the AuNP that are attributed to the molecular wire. Typically, the ligand composition of a AuNP is determined using the nanoparticle death reaction where a small amount of elemental iodine is added to an NMR sample tube containing AuNPs. This causes the AuNPs to aggregate and release the ligands into solution for sharper spectral peaks. This is more beneficial in ligand systems where the ligands have similar chemical shifts in NMR. However, upon performing this reaction, wired gold nanoparticles exhibit nearly identical integrations whether they are aggregated or not (Figure 3.11) due to the complete lack of overlap between the differing ligands. As such, the "death reaction" was unnecessary to quantify the ligand composition in this system.

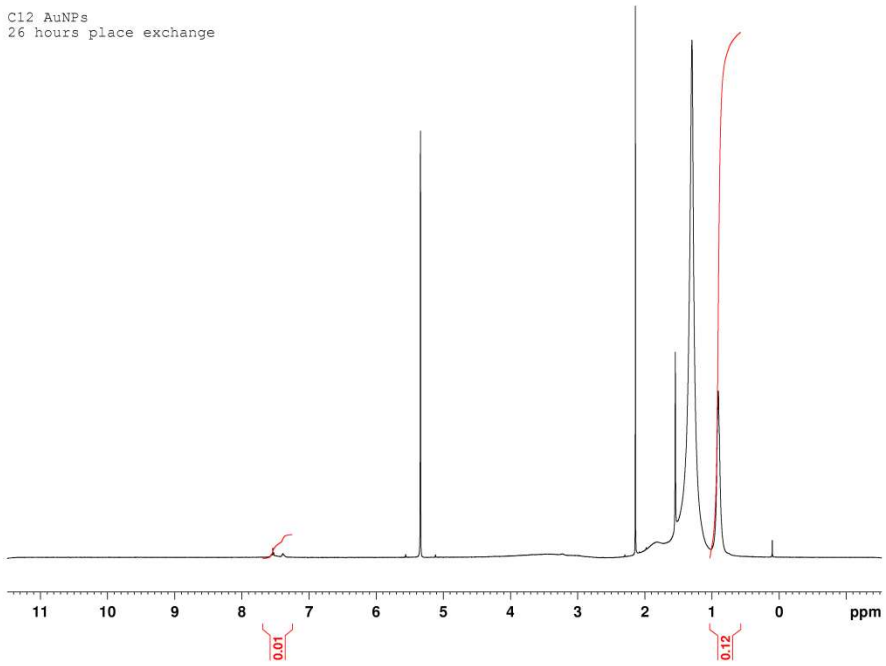

Figure 3.12. H^1-NMR of C_{12}-protected AuNPs after addition of wire molecule.

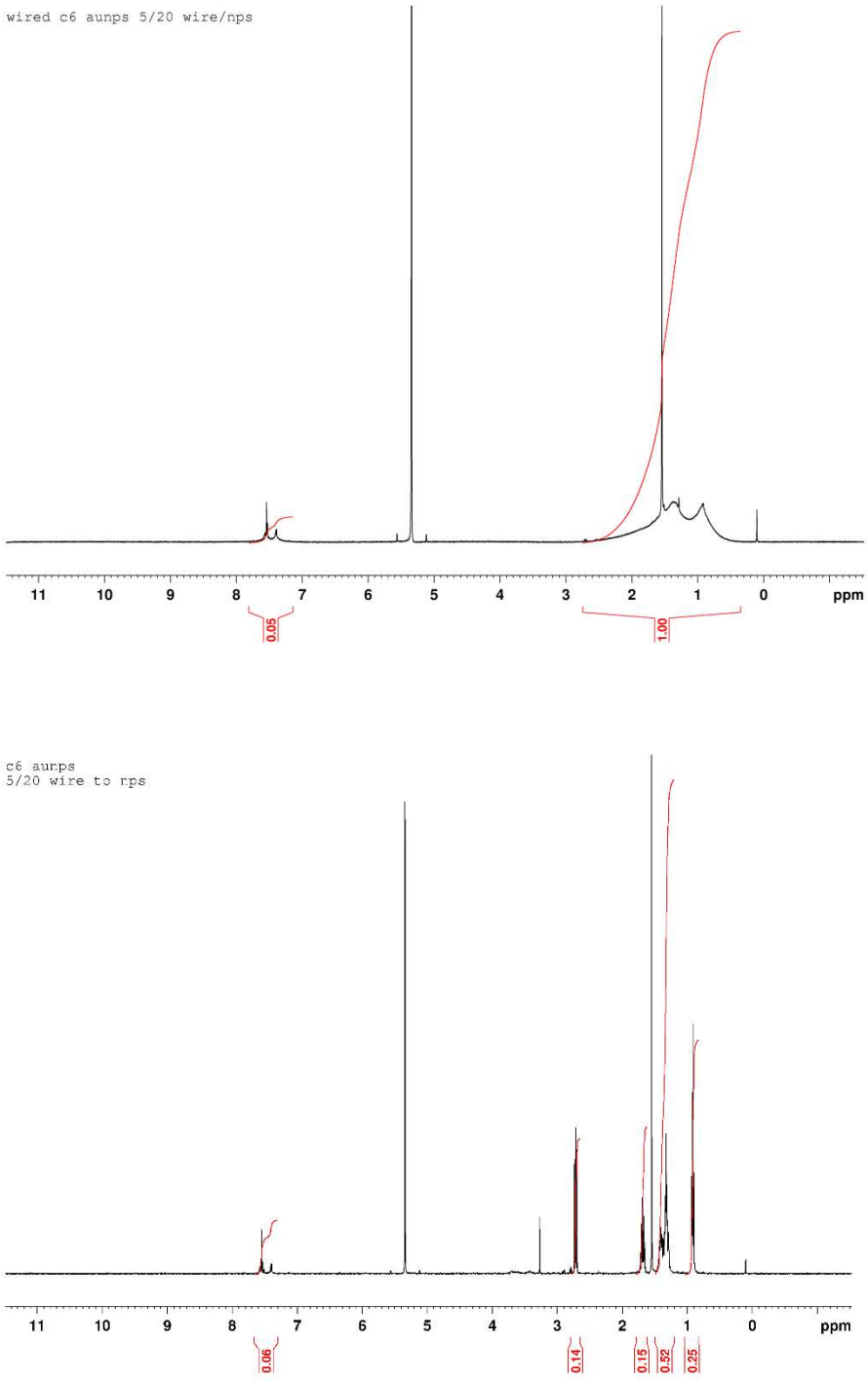

Figure 3.13. Comparison between integrations of ligands attached to the nanoparticle (above) versus detached from the particle (below) using the nanoparticle death reaction.

CHAPTER IV

EFFECT OF LIGAND CHARGE ON ELECTRON TRANSFER RATES OF WATER SOLUBLE GOLD NANOPARTICLES

Introduction

As previously discussed, organic soluble AuNPs when monodisperse can exhibit the phenomena of quantized double-layer (QDL) charging which allows them to perform as nanocapacitors.[17] While QDL charging has been difficult to demonstrate for aqueous AuNPs (due to the inability to resolve charging peaks on cyclic voltammograms[64]), water-soluble AuNPs still show potential as platforms for biological and immunological sensing as well as use in molecular circuits.[65,66] Previous work has shown that water-soluble AuNPs immobilized on the surface of an electrode and immersed in an organic solvent can present observable charging peaks.[17,67,68] Their further electrochemical properties are explored here.

Initially, monolayer-protected AuNPs were coated with organic-soluble ligands, however, experiments were soon conducted on changing the ligand to adjust the solubility of AuNPs. In 1998, Schaff et. al. used a modified Brust synthesis to synthesize AuNPs protected by glutathione[69] and Templeton et. al., synthesized AuNPs protected by N-(2-mercaptopropionyl)-glycine (tiopronin) and coenzyme A.[15] These AuNPs were the first water-soluble monolayer-protected AuNPs that could be repeatedly isolated and redissolved. One of the more interesting properties of these NPs was the retention of a pKa value similar to free ligand. Whereas significant work has been done with these NPs in the biological field,[70–78] little research has been done in discerning the electrochemical properties of water-soluble monolayer-protected AuNPs.

Results and Discussion

As discussed in Chapter 2, the SECM approach curves are graphed as normalized current (I_T) vs distance L (d/a). The equation 2.15 is then fit to the experimental data to determine the electron transfer kinetics for the AuNPs.

Measurement of glutathione- and TMA- protected AuNPs approach curves resulted in near zero positive feedback current, shown in Figure 4.1. Even under a high potential difference (1 V at the tip electrode, 0 V at the substrate), these nanoparticles continually exhibit kinetically slow electron transfer rates. This concurs with electrochemical studies on glutathione protected AuNPs which demonstrated no observable oxidation waves in cyclic voltammetry experiments. While glutathione and TMA protected AuNPs exhibited slow electron transfer, tiopronin protected AuNP approach curves demonstrate a mass-transfer limited electron transfer. This occurs at a variety of substrate potentials: unbiased, 0 V, 0.2 V, and 0.4 V with a 10 μm tip electrode. It is hypothesized that this slow electron transfer in glutathione and TMA protected AuNPs is due to the fixed ionic charge on the protecting ligands which create an electrical double layer on the outside surface of the NP.

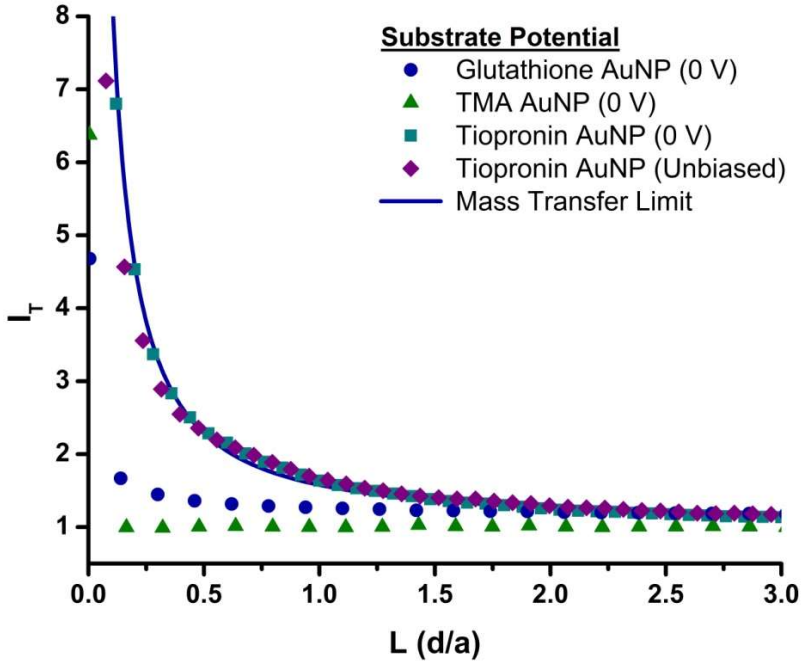

Figure 4.1. SECM (CHI 900) approach curves, Pt substrate electrode (2 mm) held at 0 V, Ag/AgCl (3 M KCl) reference, 20 mg MPC in 5 mL of 0.1 M $NaNO_3$. Glutathione-protected AuNPs with 25 µm Pt UME at 1 V. TMA-protected AuNPs with 10 µm Pt UME at 1 V. Tiopronin MPCs with 10 µm Pt UME at 0.6 V, with both 0 V and unbiased Pt substrate electrodes. Demonstrating mass-transfer limited electron transfer for tiopronin protected AuNPs and slow electron transfer rates for both glutathione and TMA protected AuNPs.

Each of the ligands investigated in this study are charged and water-soluble. It has been previously shown that the rate of electron transfer is dependent on the length of the protecting ligand.[50] Thus, the electron transfer rate for TMA protected NPs is slow since it has a length equivalent to a 12 carbon alkane chain. However, both glutathione and tiopronin have lengths equivalent to hexane or heptane and still demonstrate slower electron transfer. Our research suggests that the charge state of the passivating ligand is the dominant effect on the electron transfer rate into the gold core of water soluble AuNPs. Tiopronin and glutathione carry carboxylic

acid groups that can present a negative charge, creating additional resistance to charge transfer (Figure 4.2).

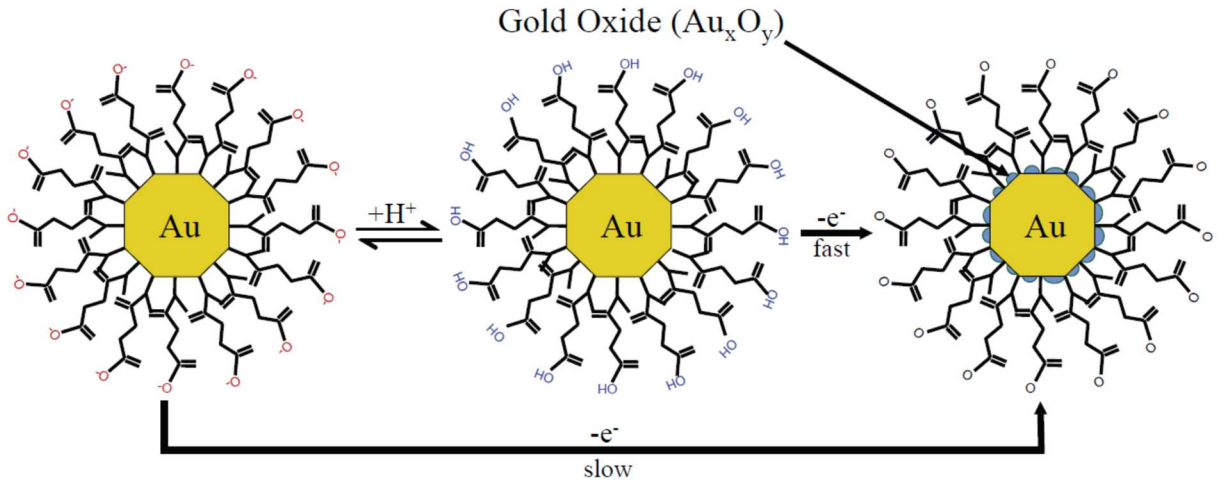

Figure 4.2. Protonated tiopronin protected NPs (center) have faster electron transfer rates because transferring electrons to form gold oxide (right) is easier than transferring electrons through the negatively charged outer shell of a deprotonated NP (left).

SECM analyses of tiopronin protected AuNPs in pH 3 and pH 5 acetate buffer with a 7 µm diameter UME show a deviation from theoretical mass-transfer theory and, thus, the electron transfer for tiopronin protected AuNPs must be kinetically limited. Because of the positive feedback curve deviation, equation (2.17) can be used to accurately describe the electron transfer of these NPs. For example, fitting equation (2.17) to the experimental data in Figure 4.3 gave a k_f value of 0.025 cm/s for tiopronin particles in pH 3 buffer and 0.003 cm/s in pH 5 buffer.

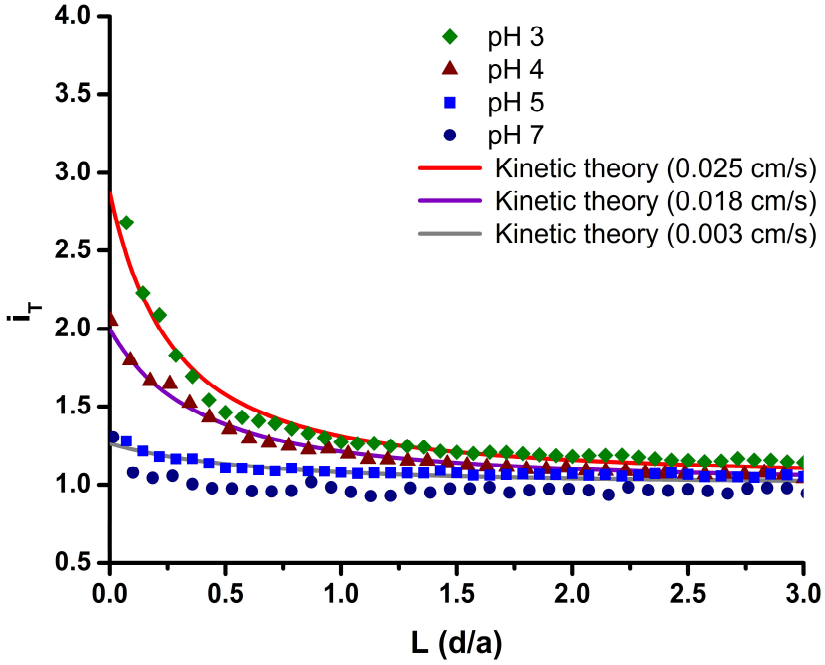

Figure 4.3. SECM (CHI 900) approach curves, 7 µm Pt UME, unbiased Pt substrate electrode (2 mm), Ag/AgCl (3 M KCl) reference, 20 mg tiopronin protected AuNPs in 5 mL of 0.1 M $NaCH_3CO_2$ buffer (pH 3, 4, and 5) and 0.1 M NaH_2PO_4 (pH 7), showing faster electron transfer rates with decreasing pH.

Because tiopronin protected AuNPs only exhibit positive feedback when UME potential was greater than 300 mV (the potential required for gold oxide formation)[79] and organic-soluble NPs exhibit positive feedback regardless of positive or negative potential on the tip electrode, it was concluded that water-soluble NPs do not transfer electrons through the same mechanism. Rather, it is thought that the branched nature of tiopronin ligands exposes the inner gold core of the nanoparticle. The exposed metallic core then forms gold oxide on its surface of the core when a potential is applied in solution. Furthermore, water-soluble NPs have never displayed QDL charging peaks, regardless of monodispersity.[80] Despite water-soluble AuNPs not exhibiting multiple charge states, they still charge their cores and can additionally transfer electrons through the formation of gold oxide. This is supported by two additional electrochemistry experiments.

First, a CV of a bare gold electrode shows the formation of gold oxide just over 300 mV (vs Ag/AgCl). This peak is still present after applying a tiopronin self-assembled monolayer to the surface of the electrode as shown in Figure 4.4.

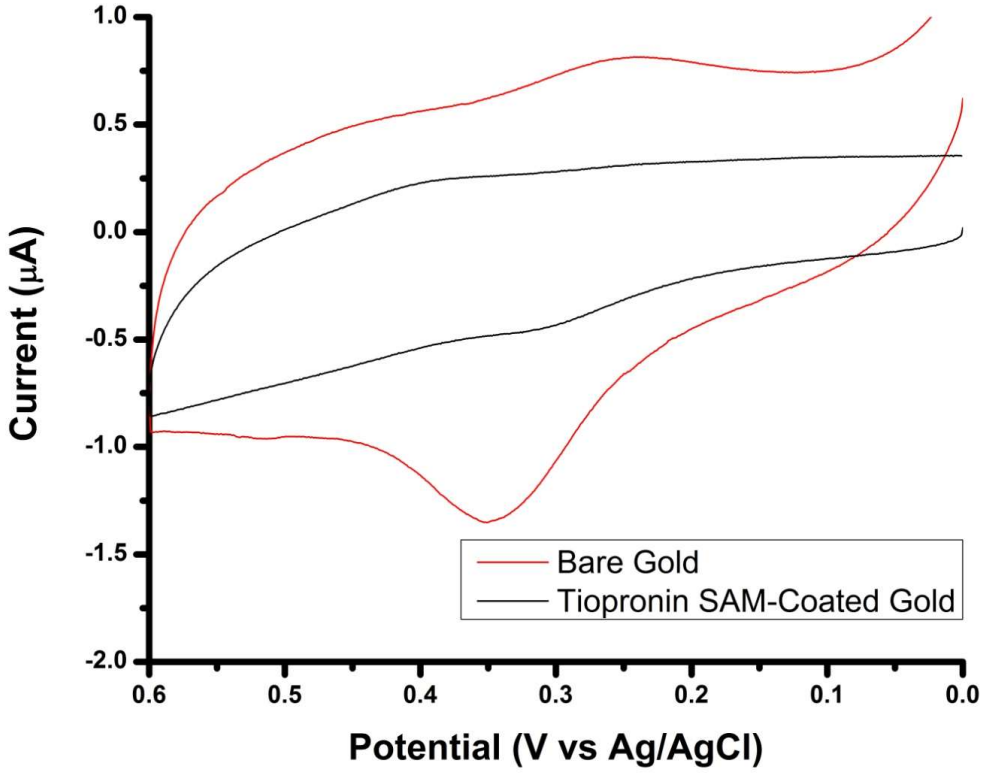

Figure 4.4. Cyclic voltammogram of a 2 mm Au macroelectrode, Ag/AgCl (Sat. KCl) reference, in 0.1 M $NaCH_3CO_2$ buffer (pH 3). In the bare gold (red line), a gold oxide peak is present between 300-400 mV.

Furthermore, while the CV of gold nanoparticles in solution shows a shift in gold oxidation formation into the solvent window, there is still a gold oxide reduction peak around 500 mV. This peak disappears after purging the solution with nitrogen, thus preventing the formation of gold oxide (Figure 4.5).

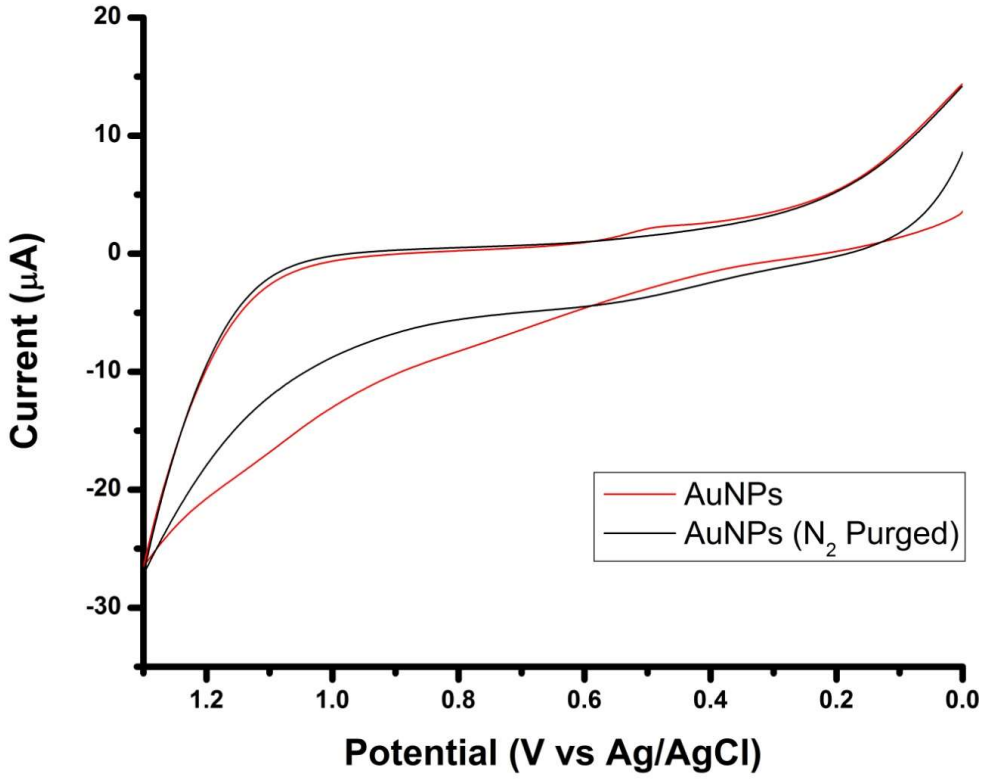

Figure 4.5. Cyclic voltammogram of tiopronin protected AuNPs (~5 mg/ml) using a 2 mm Pt macroelectrode, Ag/AgCl (Sat. KCl) reference, in 0.1 M $NaCH_3CO_2$ buffer (pH 3) showing a loss of the gold oxide reduction peak in the N_2 purged solution.

Typically, gold oxide easily forms at high pH. Despite this, the water soluble AuNPs exhibit a decrease in electron transfer when at high pH. Since pH of the system affects the ligands on the nanoparticle, this indicates that the protonation and charge of the protecting monolayer is the dominant factor of electron transfer for these NPs rather than pH alone.

The heterogeneous electron transfer rate constants for tiopronin protected AuNPs were found to be faster at lower pH (pH 3, 0.021 ± 0.001 cm/s) and much slower at higher pH (pH 9, 0.0003 ± 0.0002 cm/s) (Figure 4.4). Since the pKa of tiopronin protected NPs was determined to be approximately 4.7,[15] it is expected that there would be a dramatic change in electron transfer

rate about pH 4.7, where the percentage of protonated ligands is most sensitive to pH change. This result is demonstrated in Figure 4.6, where there is no statistical difference in electron transfer rate between pH 3 and 4 (which are both below the pKa) and a drop nearly an order of magnitude between 4 and 5 (which straddles the pKa). Furthermore, the electron transfer rate is nearly zero when approaching the higher pH levels. This is due to the majority of termini of the protecting ligands being negatively charged, almost preventing electron transfer.

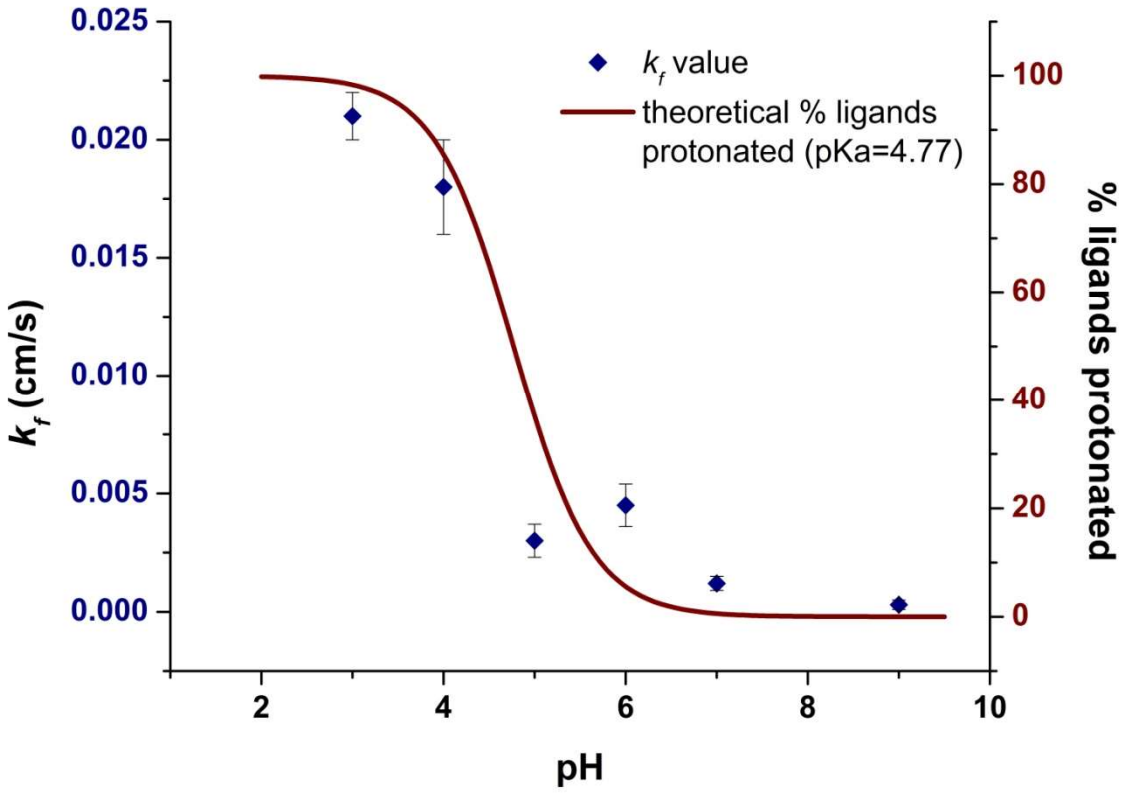

Figure 4.6. pH dependence of electron transfer rate relative to percentage of ligands protonated according to the Henderson-Hasselbalch equation, demonstrating a statistically significant drop between pH 4 and 5 in relation with the decrease in percentage of ligands protonated. The drop between pH 3 and 4 and the difference between pH 5 and 6 are statistically insignificant (n=5).

Using SECM, the electron transfer properties of water-soluble TMA, glutathione, and tiopronin protected AuNPs were determined. While TMA and glutathione-protected NPs exhibit exceedingly slow electron transfer rates, tiopronin protected NPs demonstrated measurable electron transfer rates at low pH (Table 4.1). Upon modulating the pH, the electron transfer for the tiopronin protected AuNPs can be reduced up to 2 orders of magnitude.

Table 4.1. k_f Values versus pH for tiopronin, glutathione, and TMA-protected AuNPs

Ligand	**pH**	k_f **(cm/s)** (n=5)
Tiopronin	3	0.021±0.001
	4	0.018±0.002
	5	0.0036±0.0004
	6	0.0045±0.0009
	7	0.0012±0.0003
	9	0.0003±0.0002
Glutathione	3	0.002±0.001
	4	0.0028±0.0003*
TMA	3	0.0047±0.0003*
	4	0.0046±0.0002*

*These values for k_f were calculated using the LabView program PAC_Fit.VI [81] The model used for the Tiopronin AuNPs only works on pure positive feedback. The electron transfer rate for these protecting ligands is so slow that a positive feedback is not generated (see Figure 4.1 and 4.2).

This change in the rate of electron transfer demonstrates that pH can modulate the rate due to the terminal carboxylic acid group of tiopronin. When the pH is below the pKa of the tiopronin NPs, the carboxylic acid groups are protonated and uncharged, allowing the electrons to more

easily tunnel from the tip electrode to the gold core. As the pH increases, the carboxylic groups become deprotonated and negatively charged. This results in an electrical layer of negative charge around the AuNP, inhibiting tunneling and reducing electron transfer rate. Consequently, the electron transfer rate of tiopronin protected NPs can be regulated by the pH of the solution. This ability to tune the rate of electron transfer should be applicable to other water-soluble MPCs with pH dependent functional groups. This type of electron transfer modulation through pH was further demonstrated in previous scanning tunneling microscopy studies.[82]

This work demonstrates that the dominant factor in electron transfer for water soluble gold nanoparticles is the charge on the protecting ligand. Further studies in this field must consider the electrostatic barrier resulting from the protecting ligand charge when designing nanoparticles for electron transfer.

Experimental

Materials

All reagents and materials were used as obtained unless otherwise noted. $HAuCl_4 \bullet 3H_2O$ was previously synthesized by purifying Canadian gold maple leaf coins using hydrochloric acid (99.99%).[83] Dodecanethiol, nonanethiol, hexanethiol, N-(2-mercaptopropionyl)-glycine, S-[4-(2-Phenylethynyl)phenyl]ethynylphenyl]thioacetate, acetone, ethyl ether, hexanes, tetrabutyl ammonium hexafluorophosphate, tetraoctylammonium bromide, and toluene were purchased from Sigma-Aldrich (St. Louis, MO), acetonitrile, methylene chloride, sodium phosphate (monobasic), sodium phosphate (dibasic), sodium borate, boric acid, sodium borohydride from Fisher (Fairlawn, NJ), SnakeSkin dialysis tubing was purchased from Thermo Scientific (Rockford, IL).

SECM Workstation

A CH Instruments 900 Scanning Electrochemical Microscope (Austin, TX) was used to collect approach curves and line scans. The tip electrode was a Pt UME that ranged from 7 to 25 μm in diameter. A 2 mm Pt disk electrode was used as the substrate electrode. Ag/AgCl reference electrodes were used in aqueous conditions and a Ag/Ag^+ pseudo-reference electrode was used in non-aqueous conditions. All SECM data was collected in a Faraday cage.

Before experiments were conducted, test approach curves were taken to assess the condition of the SECM electrode system. A $2.0x10^{-3}$ M solution of $FcTMA^+$ PF_6^- ((Ferrocenylmethyl)trimethylammonium hexafluorophosphate) in various buffers was used to achieve approximately 800% feedback to ensure that the system was capable of recording a maximum feedback. Buffers used were 0.1 M $NaCH_3CO_2$ (pH 3-5), 0.1 M NaH_2PO_4 (pH 6-7), and 0.1 M NaH_2BO_3 (pH 9). Furthermore, this test approach curve was used to electrochemically determine tip electrode contact.

Synthesis of Water-soluble Gold-Thiolate Nanoparticles

Gold-tiopronin nanoparticles were synthesized using slightly modified published procedures.[15] First, 0.31 g of $HAuCl_4•3H_2O$ was mixed with 0.38 g of N-(2-mercaptopropionyl)-glycine (tiopronin) in 35 ml of 6:1 v/v mixture of methanol/acetic acid. This solution was cooled to 0^o C in an ice bath. After approximately 1 h, the reaction had progressed through the first reduction process and appeared colorless. Next, 0.24 g of $NaBH_4$ in a minimal amount of water was added. The solution reacted violently and immediately turned black. After the addition of $NaBH_4$, the solution was stirred for at least 30 min in an ice bath. The methanol acetic acid mixture was then removed using rotary evaporation, forming a thick black solution. This black sludge was

dissolved in approximately 30 ml of H_2O. The pH was then adjusted to pH 1 by dropwise addition of concentrated HCl.

The dissolved AuNPs solution was then transferred into dialysis tubing and dialyzed for two to three days with water changes every 5 to 8 h until determined clean by ^{1}H-NMR. Size of AuNPs was determined through transmission electron microscopy. Organic volatile weight percentage was determined through thermogravimetric analysis (TGA).

CHAPTER V

INVESTIGATIONS OF DISSIMILARITY METAL REDUCTION PATHWAYS OF *SHEWANELLA ONEIDENSIS*

Introduction

The bacterium *Shewanella oneidensis* has been noted for its potential use in clean energy production and water purification due to its capability to metabolize a variety of substrates, including insoluble metal oxides and toxic metals.[24] This ability to transfer electrons to a material that cannot freely diffuse through the cell membrane is known as dissimilarity metal reduction (DMR). The DMR process generates a current on a variety of electrodes,[84–86] the mechanism by which DMR occurs in *S. oneidensis* has previously been investigated through electrochemical methods.

There are four non-mutually exclusive mechanisms that have been proposed to explain *S. oneidensis* DMR capabilities: direct contact, protein "nanowires," metal chelators/siderophores, and electron shuttles.[87–89] Direct contact means the process is performed on the surface of the bacterium through redox active compounds or proteins. The protein nanowires mechanism describes the bacterium's ability to grow conductive proteins that grow to a substrate. Siderophores are small molecules capable of binding to an insoluble oxidized metal and allowing it to diffuse to the bacteria. Electron shuttles work similarly but instead of solubilizing the metal, perform the redox reaction on the metal itself before diffusing back to the bacteria. While there is evidence for all four mechanisms, *S. oneidensis* demonstrates a greater reliance on soluble electron shuttles, in the form of flavins, to perform DMR.[87]

Flavins are present in much higher concentrations in *S. oneidensis* cultures as opposed to non-DMR bacteria.[31,32,90] Excess flavin has also been shown to increase *S. oneidensis* DMR

efficacy by increasing the rate of reduction.[31,91] Three additional studies support *S. oneidensis* primarily uses electron shuttles for DMR. First, iron (III) oxide was precipitated in nano-porous glass beads. Despite the pores of these beads preventing bacteria penetration, the Fe(III) oxide was still reduced.[92,93] Similarly Jiang et. al. fabricated two types of electrochemical cells: one with a 12 μm^2 window and one with a screen with holes 280 nm^2 in area.[33] Electrodes in both setups registered nearly identical currents, further confirming that direct contact is not necessary for DMR. Finally, a chronoamperometry experiment showed *S. oneidensis* bacteria producing current on an electrode. This current dramatically decreases after removing the cell media. However, upon reintroduction of the original media, the current is immediately restored.[31,33] This suggests that protein nanowires are not likely the primary mechanism for DMR and that a soluble shuttle is the dominant mechanism for *S. oneidensis* biofilms.

Although *S. oneidensis* biofilm DMR capabilities have been investigated, there is little information on the production and consumption of electron shuttles. A better understanding of the DMR mechanisms is necessary when optimizing the use of *S. oneidensis* for use in bioenergy and bioremediation applications. SECM with UMEs provides a powerful means for investigation of *S. oneidensis*.

Results and Discussion

Using electrodes as electron acceptors for respiration, *S. oneidensis* species are able to form biofilms on a variety of electrodes. As shown in Figure 5.1, a *S. oneidensis* biofilm produces a stable oxidation current on a glassy carbon (GC) electrode (+35 mV vs Ag/AgCl) after about 15 min and remains stable over a continuous 60 min growth.

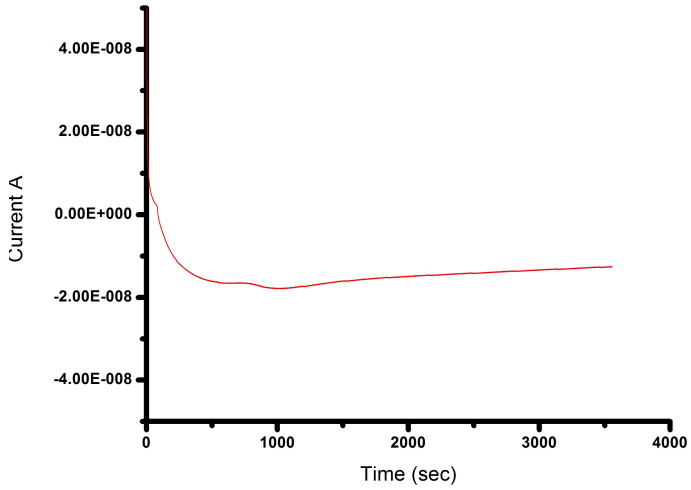

Figure 5.1. Chronoamperometry shows *S. oneidensis* biofilm formation over 60 min. The biofilm was grown on a glassy carbon electrode held at +35 mV vs Ag/AgCl

After conducting electrochemical measurements, the electrode was removed from the electrochemical cell and examined under an optical microscope. It was found that the electrogenesis of biofilms resulted in dense films of bacterial cells (Figure 5.2) whereas holding no potential on the electrode resulted in non-specific binding of much fewer cells.

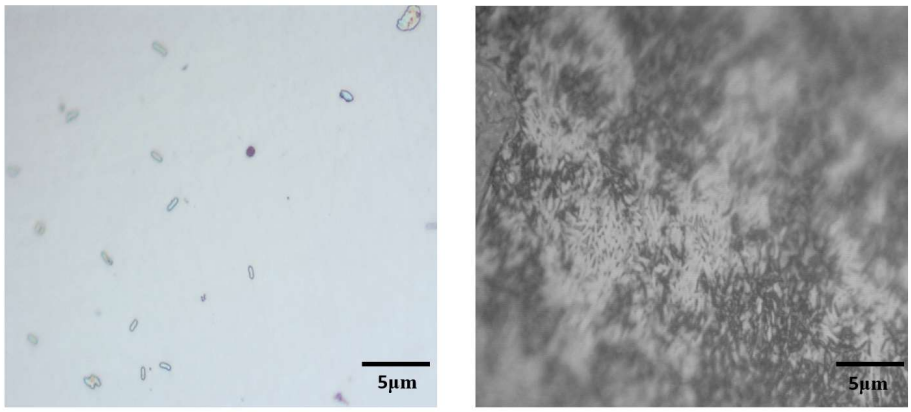

Figure 5.2. Brightfield image of 2 mm glassy carbon electrode after biofilm formation without (left) and with (right) applying potential showing increased cell density with applied potential.

Detection of Electron Shuttles

Previous work has shown that replacing the medium of a *S. oneidensis* biofilm can dramatically decrease the produced current, however, reintroducing the biofilm's original media restores the current.[31] This experiment suggests that the biofilm produces a soluble mediator, or electron shuttle, to perform redox reactions on substrates. In order to identify the electron shuttle, two techniques were used: liquid chromatography-mass spectrometry (LC-MS) and square wave voltammetry (SWV).

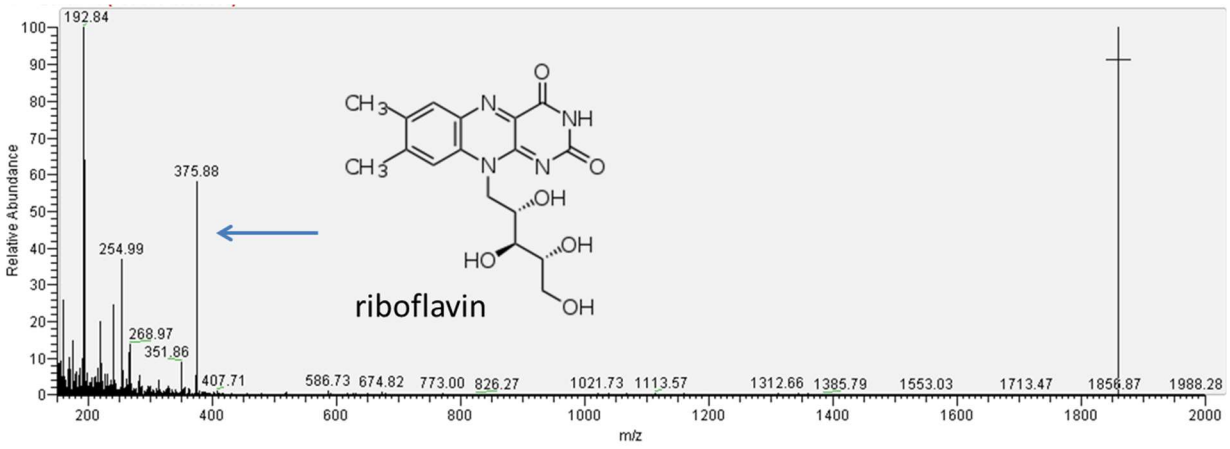

Figure 5.3. LC-MS results of riboflavin produced from *S. oneidensis* biofilm.[94]

Previous work has identified the electron shuttle using LC-MS.[94] The supernatant of a biofilm grown for 60 min was tested. In Figure 5.3, there is a mass-to-charge ratio (m/z) equal to 376, the m/z of riboflavin. Riboflavin has previously been shown as a soluble redox mediator and is a good candidate for the electron shuttle (Figure 5.4).

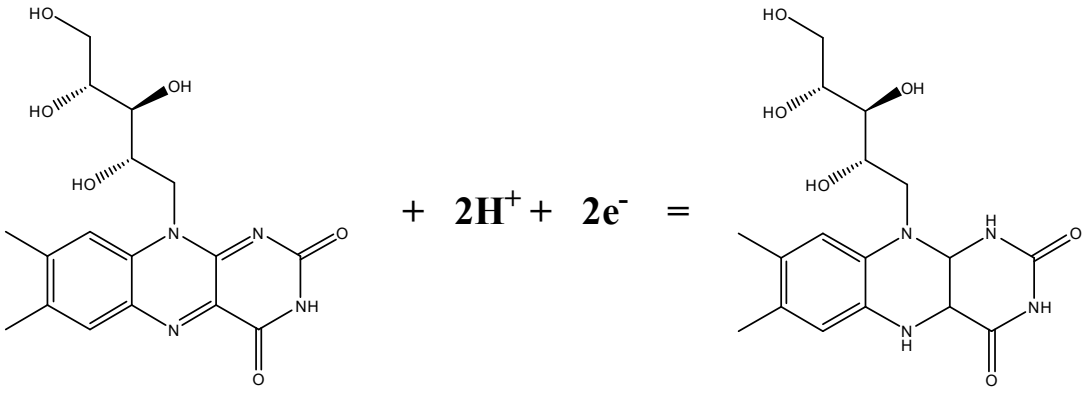

Figure 5.4. Two-electron half reaction of riboflavin.

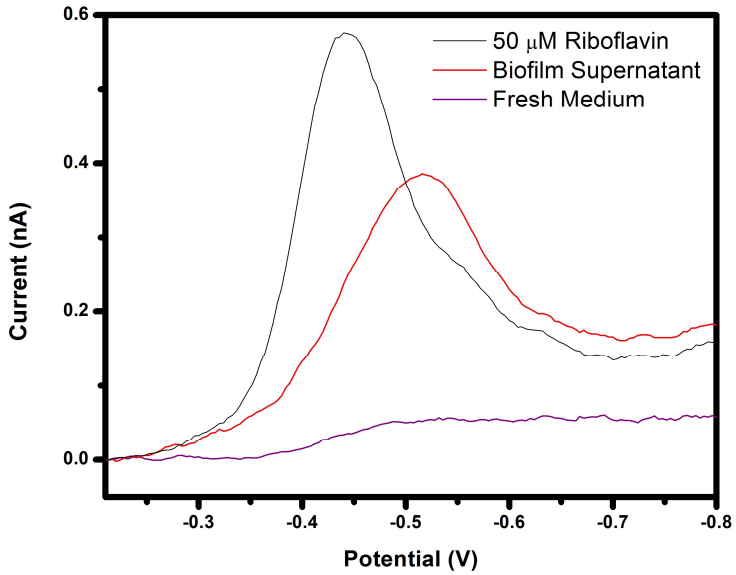

Figure 5.5. Square wave voltammogram of riboflavin produced by *S. oneidensis* MR-1 biofilm and 50 μM riboflavin.

With the electron shuttle identified, we ensured detection of the molecule electrochemically using square wave voltammetry (SWV). As shown in figure 5.5, two samples,

fresh media spiked with riboflavin and media extracted after biofilm formation, have similar reduction potentials and voltammogram shapes. The shifted potential in the biofilm media is likely due to slower electrode kinetics from partial blocking of the electrode by non-specific binding of matrix components of the supernatant. These findings were consistent with previous work on *S. oneidensis* biofilms.[31]

Time Point Detection of Riboflavin

First, a riboflavin concentration calibration curve was obtained by recording the peak current of SWV of various riboflavin concentrations in *S. oneidensis* media[94] using a 7 μm carbon fiber tip. By measuring the peak currents, the following calibration curve was created (Figure 5.6)

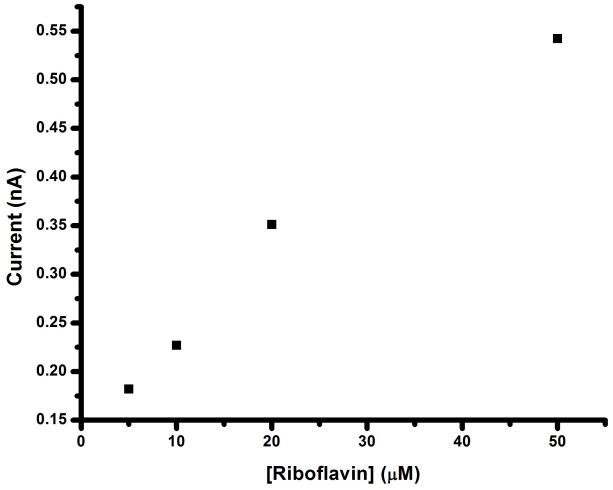

Figure 5.6. Calibration curve of riboflavin concentrations using SWV.
$i_p = (1.15 \pm 0.08) \times 10^{-12} \times [\text{riboflavin}] + (1.20 \pm 0.01) \times 10^{-10}$

After forming a biofilm on a GC electrode for 1 h, the cell media was removed and fresh media was added. This is time point 0 min in Figure 5.7.

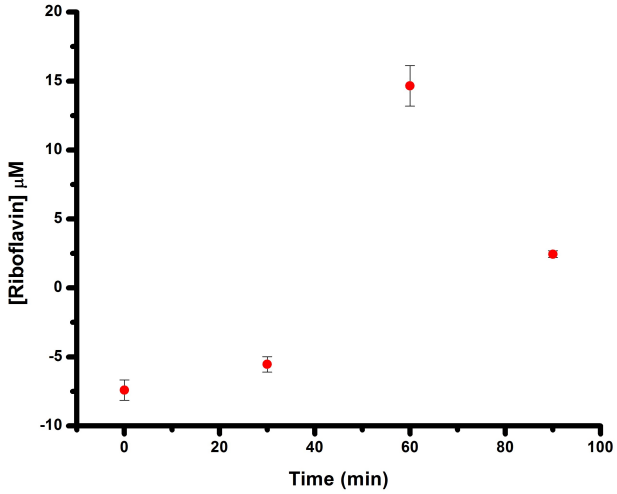

Figure 5.7. Plot of time point quantitative detection of riboflavin concentration over a *S. oneidensis* biofilm as a function of time.[94]

Figure 5.7 shows the formation of riboflavin by the biofilm as a function of time over the course of 90 min. The concentration of riboflavin secreted by the biofilm increases for the first 60 min before decreasing. Previous studies have shown that *S. oneidensis* films can be stable for long periods of time and increase riboflavin concentrations for up to 72 h. However, under these experimental conditions, the biofilm appears to stagnate or decay after only 1 h. An additional experiment showed the current steadily rising over the course of the 90 min but at concentrations far lower than expected (all measurements below the LOD of the calibration curve). The experimental conditions used were not completely hospitable to the *S. oneidensis* biofilm. Without temperature control or a rigorous maintenance of an anaerobic environment, the biofilm was not as robust as previous work. More frequent time points were able to reveal an interesting pattern in the riboflavin concentration (Figure 5.8). While the riboflavin concentration is steadily increasing over the course of the 90 min, there is a cyclical nature of increasing and decreasing current

response. This is evidence that the biofilm does not continually produce electron shuttles, but rather, has production and consumption cycles.

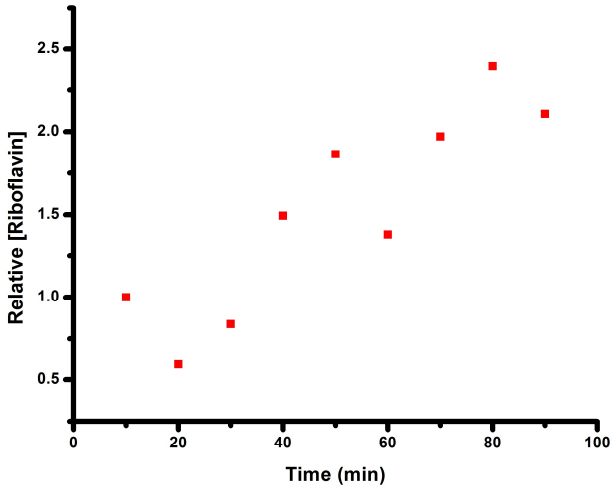

Figure 5.8. Plot of time point measurements of relative riboflavin concentration over a *S. oneidensis* biofilm as a function of time.

The lack of effective quantitation is due to the lack of sensitivity of the calibration curve. The use of a UME in a biological system lends itself to complications from the media due to biofouling, or the adsorption of biological matter on the surface of the electrode. As such, a separate calibration curve has been shown to not be an effective means of quantitation. Instead, standard addition should be employed at the end of each experiment to accurately measure low concentrations using square wave voltammetry.

Real-time Measurements

Real-time measurements of riboflavin concentration were conducted in order to elucidate the riboflavin production/consumption cycle. By poising the tip electrode above the biofilm and biasing the substrate to induce biofilm growth, the current generated on the tip electrode will

correspond to changes in riboflavin concentration. As shown in Figure 5.9, the overall current response peaks in the first 20 min and decreases over the course of the 60 min but not before temporarily rising around 40 min. This confirms some production/consumption cycle of the *S. oneidensis* biofilm.

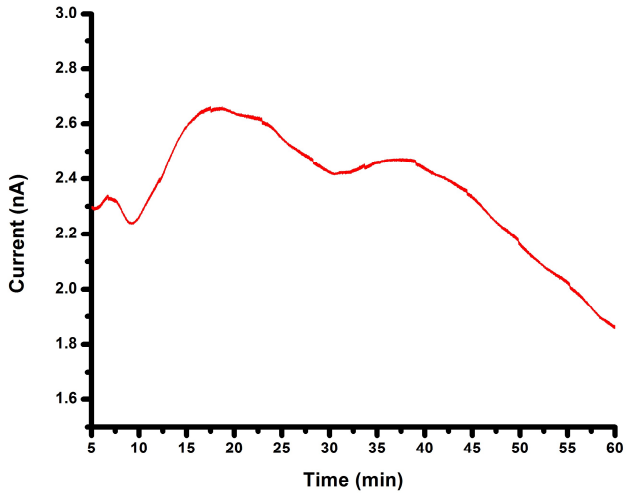

Figure 5.9. Real-time measurement of current response to riboflavin production and consumption.

X-Scan

Figure 5.10 shows the normalized current over a *S. oneidensis* biofilm with additional riboflavin and FcTMA redox mediators added to fresh media. As the tip electrode measures the current above the exposed glassy carbon electrode substrate, the current generated corresponds to the concentration of mediator (riboflavin or FcTMA). However, as the tip moves above the biofilm, the concentration of mediator decreases as the biofilm consumes riboflavin leading to an approximately 40% decrease in current. This decrease in current is not present in FcTMA as the biofilm is unable to utilize this mediator in respiration. This demonstrates the specificity of *S. oneidensis* to use riboflavin over different electron shuttles.

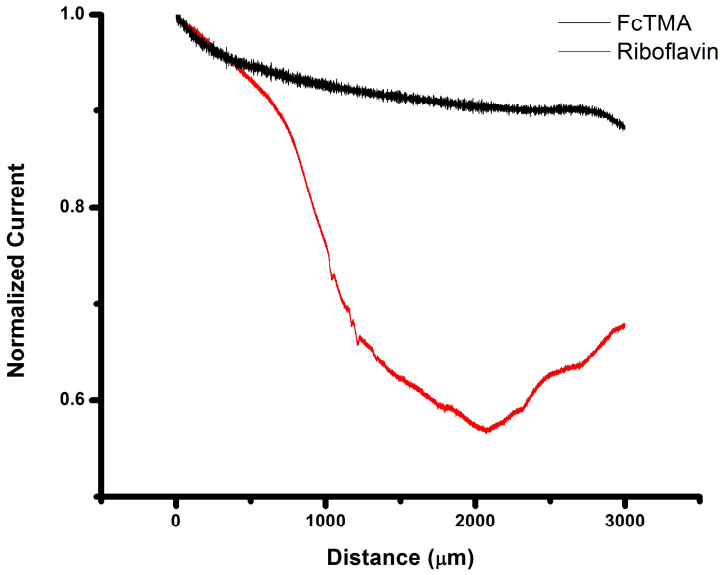

Figure 5.10. Normalized current changes of an SECM x-scan over masked *S. oneidensis* biofilm in additional riboflavin and FcTMA. Tip potential was held at -0.6 V in riboflavin and +0.6 V in FcTMA.

2D Images

By utilizing the same x-scan technique discussed above, a two-dimensional image of the biofilm can be created by stacking multiple x-scans, or rastering across the surface. For the image generated in Figure 5.11, a biofilm was grown using a masked electrode. After the mask was removed, minimal media spiked with 20 μM riboflavin was added to increase the signal current, and the tip electrode was held at -0.6 V to measure riboflavin reduction current. The substrate electrode was held at 0.035 V to induce biofilm growth.

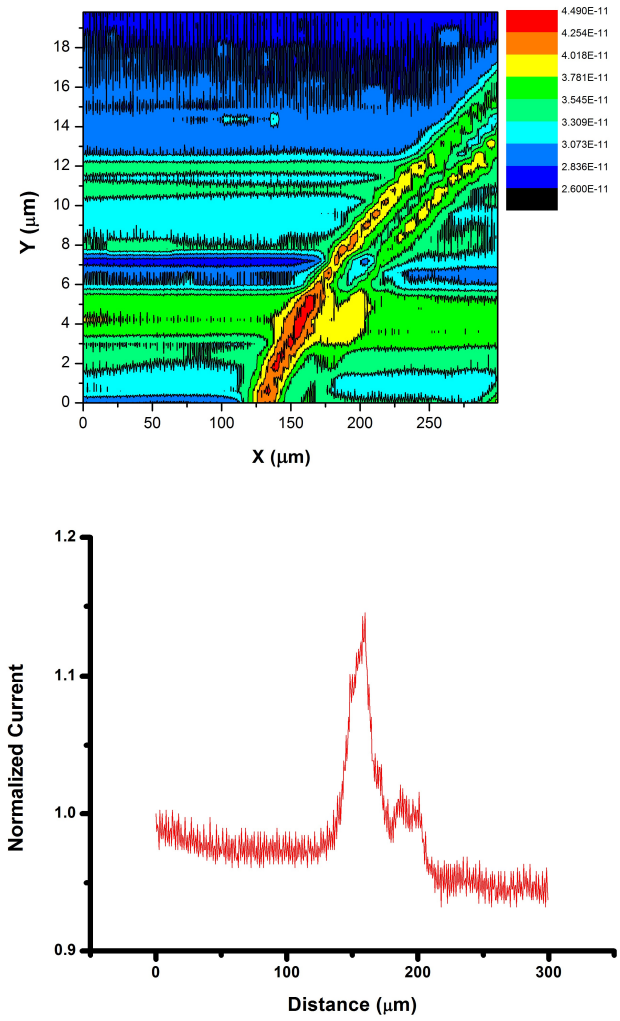

Figure 5.11. 2D image of a masked *S. oneidensis* MR-1 biofilm (left) and a line scan at Y=4.2 (right) in excess riboflavin. There is up to an 11% increase in signal current above the biofilm.

After rastering across the biofilm, there is an increase in signal current over the biofilm versus over the substrate. However, the area of the increase in current is much smaller than expected and is only about 100 μm in width. This is far smaller than the 1 mm mask used during biofilm growth, indicative of riboflavin production "hot spots." Instead of the entire biofilm continuously producing and consuming riboflavin, only certain bacteria on the film are tasked with riboflavin production. As Figure 5.10 shows below, these "hot spots" remain even if the entire electrode is covered in biofilm. Using the same parameters as Figure 5.11, the image in Figure

5.12 shows increased riboflavin concentrations over particular areas of the biofilm. The image is not uniform and, as such, demonstrates the production and consumption of a film are non-uniform.

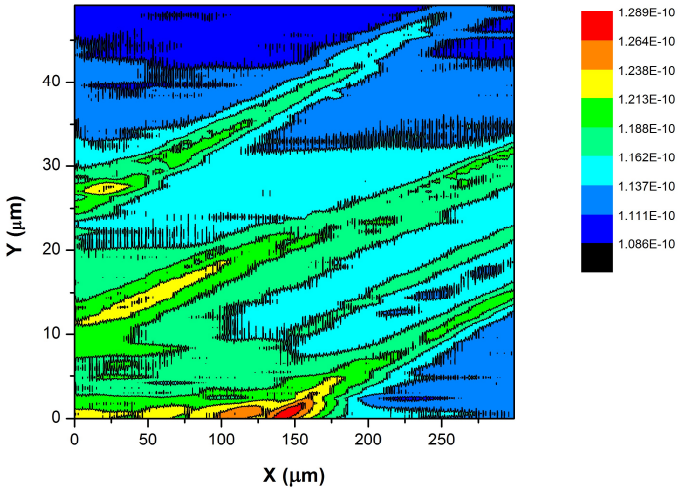

Figure 5.12. 2-D image of a non-masked *S. oneidensis* MR-1 biofilm in excess riboflavin. Despite not being masked, there is a 20% increase in signal current above certain "hot spots" of the biofilm.

TSP-C

After the above experiments were conducted, a new strain of *S. oneidensis* was studied: TSP-C. *S. oneidensis* TSP-C is a rifampicin resistant strain. During the liquid culture, the LB broth contained rifampicin (10 µg/mL). A growth curve was created to ensure bacteria were extracted from the culture during the log phase. According to the growth curve shown in Figure 5.13, the log phase of *S. oneidensis* TSP-C is between 2 and 20 h. Bacteria were collected after 12 h for biofilm growth experiments. It was expected that *S. oneidensis* TSP-C would produce biofilms and riboflavin in a similar manner to the MR-1 strain.

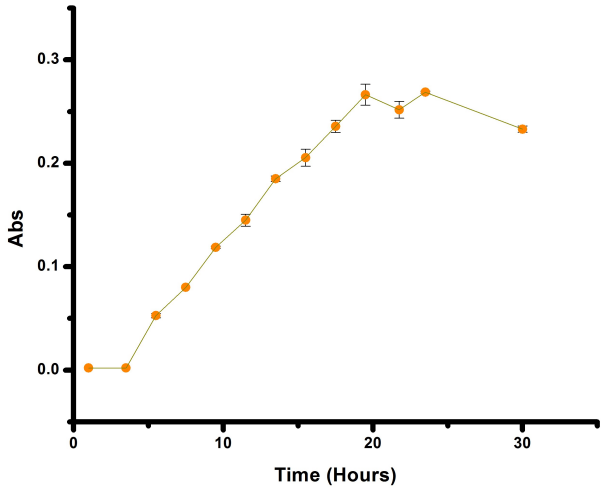

Figure 5.13. Growth curve for *S. oneidensis* TSP-C demonstrating the midpoint of the log phase to be approximately 12 hours after inoculation.

Unfortunately, we were unable to reproduce the biofilm formations of MR-1 using TSP-C. In most cases, a biofilm was never produced using the same parameters for MR-1 biofilm growth. In the cases of biofilm production, it did not adhere as strongly to the GC electrode and immediately lifted during media changes.

Furthermore, it was confirmed through SWV (Figure 5.14) that the TSP-C biofilms were not producing riboflavin during the biofilm formation as neither fresh medium nor supernatant collected after biofilm formation exhibited the characteristic riboflavin peak at -450 mV. TSP-C is not an appropriate substitute for MR-1 for investigations of DMR experiments.

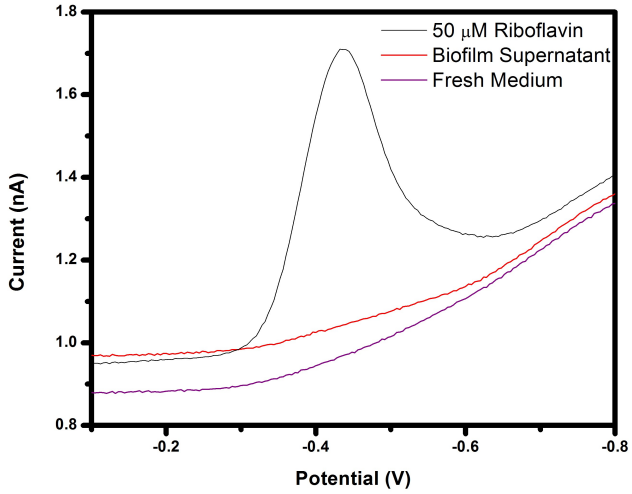

Figure 5.14. SWV of supernatant of *S. oneidensis* TSP-C biofilm after 60 min formation, fresh media, and 50 μM riboflavin in media indicating no riboflavin production.

Experimental

Materials

Chemicals were used as purchased. Riboflavin, sodium lactate, and fumarate were purchased from Sigma Aldrich. The medium salts were purchased from Fisher and Sigma Aldrich.

Microbiological Methods

S. oneidensis MR-1 and TSP-C were provided by the Elliott research group from Boston University. Both strains were grown from -80°C glycerol frozen stock by culture on lysogeny broth agar plates (35 g LB agar per 1 L water) for 24 h. 3 mL of LB broth (Sigma-Aldrich) was inoculated and then placed in a 175 rpm shaker overnight at 30°C. This culture was centrifuged at 6000 rpm for 10 min to remove supernatant. The cells were then resuspended in minimal media.

Minimal media was prepared according to previous literature.[31] Before running experiments, around 25 mL of media was purged with N_2 for 60 min after the addition of 20 mM sodium lactate and 20 mM fumarate.

Analytical Methods

Electrochemical measurements were performed using a CHI 900 SECM from CH Instruments. The tip electrode was a 7 μm carbon fiber tip fabricated in house. The counter electrode was a Pt wire and the reference electrode was Ag/AgCl.

In order to form the biofilm using electrogenesis, *S. oneidensis* cells were first suspended in minimal media (as described above) and then added to an electrochemical cell. The electrode was held at 35 mV (vs. Ag/AgCl) for one hour.[95] After the biofilm was formed, the media was removed and excess cells were removed using centrifugation. The supernatant was added back to the electrochemical cell and an approach curve was performed to determine the distance (the tip electrode was held at -0.6 V and the substrate held at -0.2 V vs Ag/AgCl). Experiments were conducted 20 μm away from the surface of the biofilm.

To detect riboflavin, SWV was used with the following parameters: initial potential, -0.2 V; final potential, -0.8 V, increment potential, 4 mV; amplitude, 25 mV; frequency, 15 Hz.

For X-scan and 2D measurements, the biofilm was grown on a masked electrode with a 1 mm wide strip exposed. The mask was removed and the electrode was visually inspected for the presence of cells. After approaching the substrate, the tip electrode was rastered across the surface 20 μm away from the substrate. The tip was held at -0.6 V for riboflavin and +0.6 V for FcTMA.

LC-MS was conducted by Dr. C. Ruth McNees in the Bachmann research group. The cell-free supernatant was analyzed using electrospray ionization-triple quadrupole in both positive and negative scan modes at 150-2000 m/z ratio.

CHAPTER VI

CONCLUSIONS AND FUTURE WORK

Summary

In this thesis, we have demonstrated the use of scanning electrochemical microscopy as an effective tool for analyzing electron transfer kinetics of gold nanoparticles (AuNPs). We further demonstrated SECM as a means of spatially detecting electron shuttles produced by *Shewanella oneidensis* biofilms. In Chapter I, we discussed not only the motivations behind these investigations: the need to improve and develop renewable energy sources, but also the potential for gold nanoparticles and *S. oneidensis* to work towards those goals. In Chapter II, we discussed the theory behind SECM and its capabilities for analyzing both nanoparticles and bacteria.

Chapter III described the investigations of electron transfer rates for organic-soluble AuNPs. By coating the NPs in a non-conducting alkanethiolate monolayer, these NPs were shown to act as nanocapacitors. In order to use these NPs in as nanocapacitors, molecular wires are necessary for connections. It was shown that one particular molecular wire, S-[4-(2-Phenylethynyl)phenyl]ethynylphenyl]thiol, or PEPEPSH, was capable of being added to various nanoparticles. Interestingly, the addition of the molecular wire increases electron transfer rates for longer protecting ligands (dodecanethiolate- and octanethiolate-protected NPs), while the electron transfer rates of shorter hexanethiolate-protected AuNPs were actually slowed compared to unwired NPs. This evidence suggests that the rigidity and length of the wire contributes to an increased tunneling distance for the electrons travelling from inside the NP to the electrode.

Chapter IV discussed the use of SECM to measure the electron transfer rate of water-soluble AuNPs in a similar manner to Chapter III. It was found that water soluble AuNPs transfer electrons through the formation of gold oxide on the surface of the NP. While the electron transfer

rate of glutathione- and TMA- protected NPs were found to be slow, tiopronin-protected NPs had faster electron transfer rates. It was found that the electron transfer rate of tiopronin-protected AuNPs was pH dependent and could be slowed with increasing pH. The work presented here demonstrates that the negative charge on a protecting ligand creates an electrostatic barrier that slows electron transfer and that nanoparticles with neutrally charged ligands exhibit faster electron transfer rates.

In Chapter V, the capabilities of *S. oneidensis* biofilms were analyzed using SECM, confirming the secretion of riboflavin as an electron shuttle that facilitates the *S. oneidensis* capability of reducing insoluble metals. By measuring the current generated on the tip electrode, we confirmed that riboflavin could be detected electrochemically and have promising preliminary results towards quantifying concentration in cell media using square wave voltammetry. Spatial scanning of biofilms grown on electrodes showed selective consumption of riboflavin over other electrochemical mediators as well as non-uniform riboflavin production. The importance of using the specific *S. oneidensis* MR-1 strain was also discovered, as the variant TSP-C strain did not exhibit the biofilm formations nor the production of riboflavin.

Future Directions

Wired AuNPs

Quantitative analysis of the amount of wire exchanged onto nanoparticles needs to be developed as the combination of TEM, TGA, and ^{1}H-NMR are only capable of giving a qualitative estimate of the amount of wire added to a AuNP. In order to get a more definitive result, the use of matrix assisted laser desorption ionization, ion mobility, mass spectrometry (MALDI-IM-MS) would be beneficial. Using a technique previously developed in the lab by Dr. Kellen Harkness,

MALDI-IM-MS is capable of not only determining the amount of wire added to a NP, but can also provide information as to the relative distribution of the ligand.[96] By synthesizing heavily place exchanged nanoparticles, we can use MALDI-IM-MS to determine if molecular wires phase segregate and collect on a single face of a NP or if they add randomly to the entire surface. Preliminary results using 2D ^{1}H-NMR suggests that the wires add randomly to the entire surface.

Additionally, introduction of wire molecules on the nanoparticles in films could enhance electron transfer rates. The conductivity of AuNP films created from both wired and unwired particles will be measured using a four point probe. We hypothesize that there will be a measurable increase in conductivity in the former as the wires should be able to facilitate faster electron percolation through the film.

A shorter wire was synthesized (Appendix B) in order to demonstrate increased electron transfer rates on the hexanthiolate-protected AuNP, but the wire did not place exchange onto the AuNPs. Further experiments should be conducted on AuNPs with longer protecting ligands, such as hexadecanethiolate, to determine the effect on electron transfer rates when the molecular wire, PEPEPSH is incorporated into the monolayer.

pH-sensitive AuNPs

With the electron transfer rate of tiopronin-protected AuNPs well understood, the next step for this project would be to begin integration into a photosystem I solar cell. The ability of NPs to act as both a solid state mediator as well as capacitors for the photoactive protein is currently undergoing preliminary investigation.

Shewanella oneidensis

This work requires an increase in imaging resolution and reproducibility. Because of the variable nature of the bacterial growth process, further steps should be taken to ensure growth conditions are identical between experiments. According to Zhang et. al., the conditions for successfully and consistently growing a *S. oneidensis* biofilm in an electrochemical cell are discussed below.[97]

The culture in LB broth is identical to the procedure in Chapter V, however, the extraction of cells from the culture occurs at the start of the stationary phase (20 h), rather than the middle of the log phase (12 h).

The medium used during electrochemical measurements is slightly different containing 0.46 g NH_4Cl, 0.225 g K_2HPO_4, 0.225 g KH_2PO_4, 0.225 g $(NH_4)_2SO_4$, 20 mM HEPES, 0.5 g casamino acids, 10 mL Wolfe's mineral mix and 10 mL Wolfe's vitamin mix per liter with a pH of 7.2. The bacteria is added to the basal medium with an additional 100 mM filter-sterilized sodium lactate. Bacteria were grown on a gold electrode at a bias of +0.04 V vs Ag/AgCl. The electrochemical cell was covered in parafilm and continuously sparged with nitrogen to maintain an anaerobic environment. Sparging was only halted during electrochemical measurements. Zhang et. al. used an additional redox mediator, 0.5 mM $Ru(NH_3)_6Cl_3$, rather than the riboflavin that is naturally produced by the biofilm.

Using the identical strain (MR-1) under the more optimized conditions described above should provide even more informative results. With increased bacterial stability and consistency, the eventual goal of monitoring the electron shuttle consumption and production on an individual bacterium can also be worked towards.

APPENDIX A

SQUARE WAVE VOLTAMMETRY

Square wave voltammetry (SWV) is a voltammetric technique used to minimize the effect of non-faradaic current.[35] Rather than the constant change in potential of a linear sweep voltammogram, a square wave potential waveform is an increasing square wave (Figure A.1.)

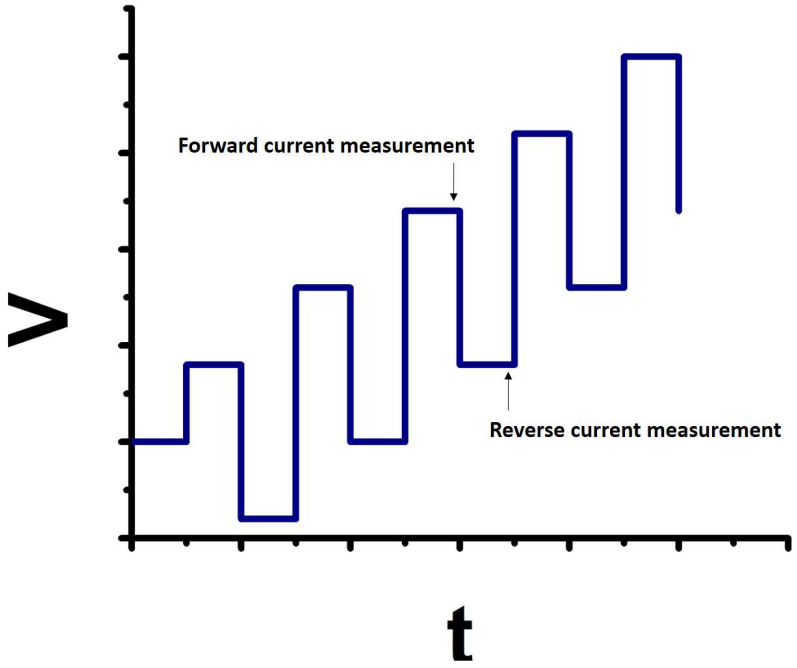

Figure A.1. Potential waveform for square wave voltammetry

Current is measured at two time points: at the end of the forward potential pulse and at the end of the reverse potential pulse. The difference between these two currents is graphed versus the voltage on a SWV. One major advantage of SWV is the background suppression from negating non-faradaic, or capacitive, current. By pulsing the voltage and performing the reverse process, there is no charging contribution as any double layer formation is immediately cancelled.

APPENDIX B

POSITIVE FEEDBACK APPROACH CURVE FITTING

Analytical Method

The following describes the use of excel to fit Equation (2.17) to experimental data to find the k_f of an analyte.

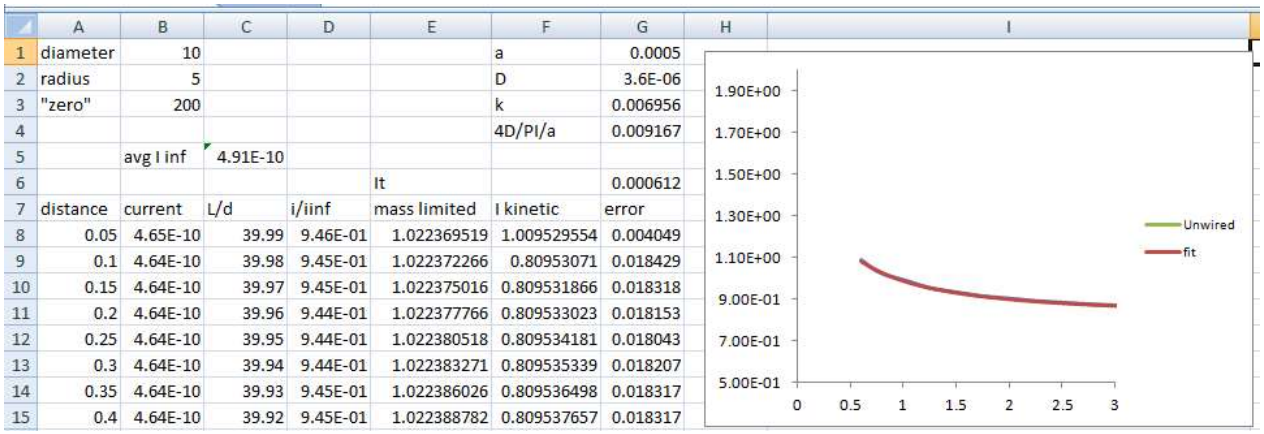

	A	B	C	D	E	F	G
1	diameter	10				a	0.0005
2	radius	5				D	3.6E-06
3	"zero"	200				k	0.006956
4						4D/PI/a	0.009167
5		avg I inf	4.91E-10				
6					It		0.000612
7	distance	current	L/d	i/iinf	mass limited	I kinetic	error
8	0.05	4.65E-10	39.99	9.46E-01	1.022369519	1.009529554	0.004049
9	0.1	4.64E-10	39.98	9.45E-01	1.022372266	0.80953071	0.018429
10	0.15	4.64E-10	39.97	9.45E-01	1.022375016	0.809531866	0.018318
11	0.2	4.64E-10	39.96	9.44E-01	1.022377766	0.809533023	0.018153
12	0.25	4.64E-10	39.95	9.44E-01	1.022380518	0.809534181	0.018043
13	0.3	4.64E-10	39.94	9.44E-01	1.022383271	0.809535339	0.018207
14	0.35	4.64E-10	39.93	9.45E-01	1.022386026	0.809536498	0.018317
15	0.4	4.64E-10	39.92	9.45E-01	1.022388782	0.809537657	0.018317

Pictured above, the excel file should be available in the Cliffel lab archive. If unavailable, set up is described below.

Constants

	A	B	C	D	E	F	G
1	diameter	10				a	0.0005
2	radius	5				D	0.0000036
3	"zero"	200				k	0.00695599
4						4D/PI/a	0.00916732
5		avg I inf	4.91E-10				

In the upper left hand corner, the highlighted sections above indicate the constants in the equations. “Diameter” is the diameter of the UME used in the experiment in µm, and the excel sheet automatically uses the radius. This number is acquired from visual measurement using a

microscope. “Zero” is the distance that the tip electrode would have to travel to make contact with the substrate electrode (also in µm). CHI software records the data as distance travelled by the tip versus tip current, so the “zero” value is necessary to correctly graph the system as an approach curve. D is the known diffusion coefficient in cm^2/s.

	A	B	C	D	E	F	G
1	diameter	10				a	0.0005
2	radius	5				D	0.0000036
3	"zero"	200				k	0.00695599
4						4D/PI/a	0.00916732

Highlighted in blue above are the calculated constants based on the inputs.

The radius formula is

```
=B1/2
```

a must be in cm to match the units, the formula is

```
=B2*0.0001
```

4D/PI/a is

```
=4*G2/(PI()*G1)
```

Input Data

After converting a CHI file to a text file, the data is pasted into the distance and current columns, highlighted below in orange.

1	diameter	10				a	0.0005
2	radius	5				D	0.0000036
3	"zero"	200				k	0.00695599
4						4D/PI/a	0.00916732
5		avg I inf	4.91E-10				
6					It		0.00061204
7	distance	current	L/d	i/iinf	mass limited	I kinetic	error
8	0.05	4.65E-10	39.99	9.46E-01	1.022369519	1.009529554	0.00404924
9	0.1	4.64E-10	39.98	9.45E-01	1.022372266	0.80953071	0.01842922
10	0.15	4.64E-10	39.97	9.45E-01	1.022375016	0.809531866	0.0183185
11	0.2	4.64E-10	39.96	9.44E-01	1.022377766	0.809533023	0.01815319
12	0.25	4.64E-10	39.95	9.44E-01	1.022380518	0.809534181	0.0180433
13	0.3	4.64E-10	39.94	9.44E-01	1.022383271	0.809535339	0.01820748
14	0.35	4.64E-10	39.93	9.45E-01	1.022386026	0.809536498	0.01831724
15	0.4	4.64E-10	39.92	9.45E-01	1.022388782	0.809537657	0.01831693
16	0.45	4.64E-10	39.91	9.45E-01	1.02239154	0.809538817	0.01826154
17	0.5	4.64E-10	39.9	9.44E-01	1.022394298	0.809539977	0.01815132
18	0.55	4.64E-10	39.89	9.44E-01	1.022397059	0.809541138	0.01804143
19	0.6	4.63E-10	39.88	9.44E-01	1.02239982	0.8095423	0.01798645
20	0.65	4.64E-10	39.87	9.44E-01	1.022402584	0.809543462	0.01809555
21	0.7	4.64E-10	39.86	9.45E-01	1.022405348	0.809544625	0.01825997
22	0.75	4.64E-10	39.85	9.44E-01	1.022408114	0.809545789	0.01820466
23	0.8	4.64E-10	39.84	9.44E-01	1.022410881	0.809546953	0.01809461
24	0.85	4.63E-10	39.83	9.44E-01	1.02241365	0.809548117	0.01798489

All the highlighted cells in green are calculated from the data directly using the following formulas.

L/d is the normalization of the distance value to the radius of the UME which converts distance traveled to L

```
=($B$3-A8)/$B$2
```

Avg I inf represents the i_∞ value of the equation and is an average of the cells in the current column from a L/d value ranging from 4 to 10. This varies depending on the measurements but the general formula is

=AVG(B___:B___)

i/iinf is the normalization of the measured current to the i_∞

=B8/$C$5

Mass limited is the computationally determined mass limited equation based entirely on L (Equation 2.7) and the cell formula is

=(0.68+(0.78377/C8)+0.3315*EXP(-1.0672/C8))

Calculating k_f

k_f is calculated by fitting "l kinetic"(highlighted in dark red) to the experimental data using the least squares method.

"l kinetic" is Equation (2.17). The excel formula is

=(E8*($G$4+$G$3))/((E8*$G$4)+$G$3)

The "error" column (highlighted in grey) is the square of the difference between Equation (2.17) and the experimental data.

=(D8-F8)^2

The sum of the errors is highlighted in black. The values for this formula are determined by the data. Model fits typically run from $0.5 < L/d < 3$. The general formula is

=SUM(G____:G____)

"k" is the calculated k_f based on the sum of the errors. Using excel solver, we find the best fit by minimizing the sum of the errors.

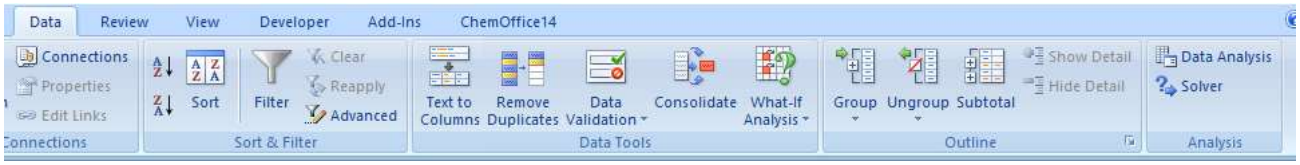

In the data tab of the excel task bar, the solver function is located in the analysis section under data analysis. If not present, it is installed through Microsoft button > excel options > add ins > analysis tool pak. When you click on solver, the following window will appear

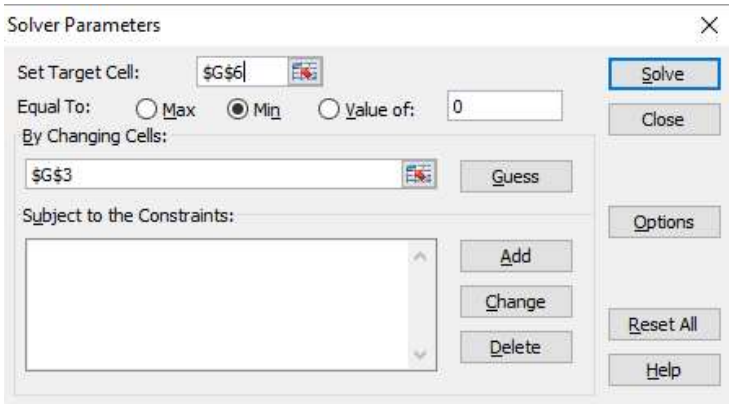

The target cell is the sum of the errors "$G$6." Set the "Equal to:" to "min." to minimize the sum of the error. Set "By Changing Cells:" to "$G$3" or the k_f value. Then click solve. Excel iterative tries k_f values and uses a generalized reduced gradient algorithm to find the minimum value for the target cell. As such, your initial guess for k_f must be close to the calculated value, otherwise, the algorithm may not converge. If it does not converge, try another k_f value. If solver finds a k_f value, it will automatically input it on cell G3.

In order to check the calculated value, graphing the data is strongly recommended to visually inspect the fit. Experimental data should have x values from column "L/d" and y values

from “i/iinf.” The kinetically limited equation should have the same x values but y values from “I kinetic.” This graph should update in real time as k_f values are changed.

For example, the initial guess for this fit is pictured here

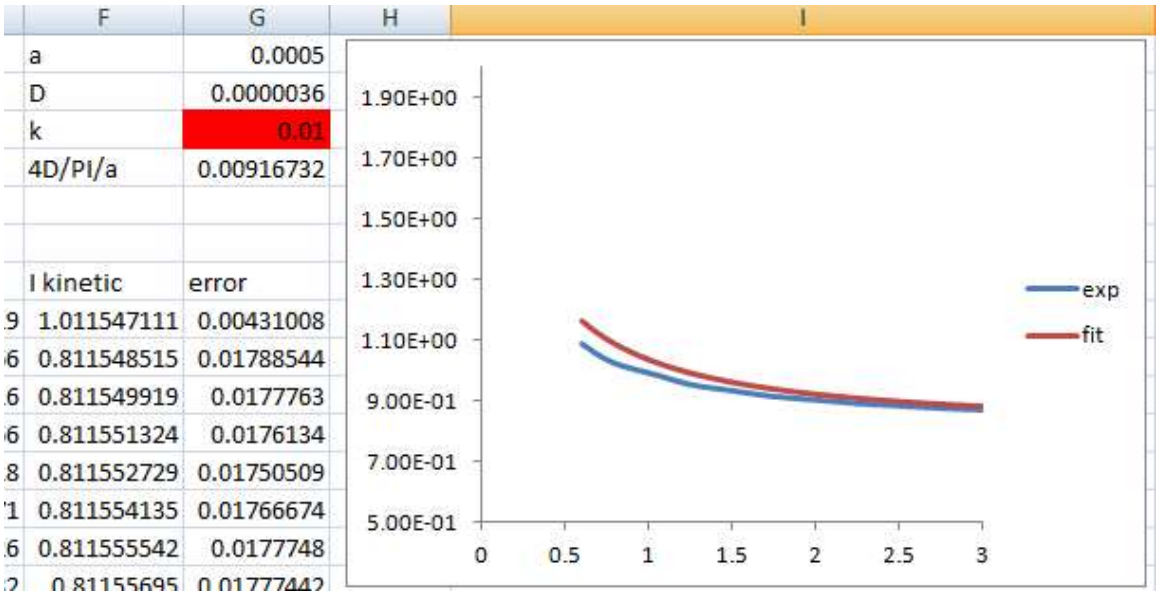

	F	G
	a	0.0005
	D	0.0000036
	k	0.01
	4D/PI/a	0.00916732
	I kinetic	error
9	1.011547111	0.00431008
6	0.811548515	0.01788544
6	0.811549919	0.0177763
6	0.811551324	0.0176134
8	0.811552729	0.01750509
1	0.811554135	0.01766674
6	0.811555542	0.0177748
2	0.81155695	0.01777442

After running solver, the fit line is moved to overlap with the experimental data completely (below)

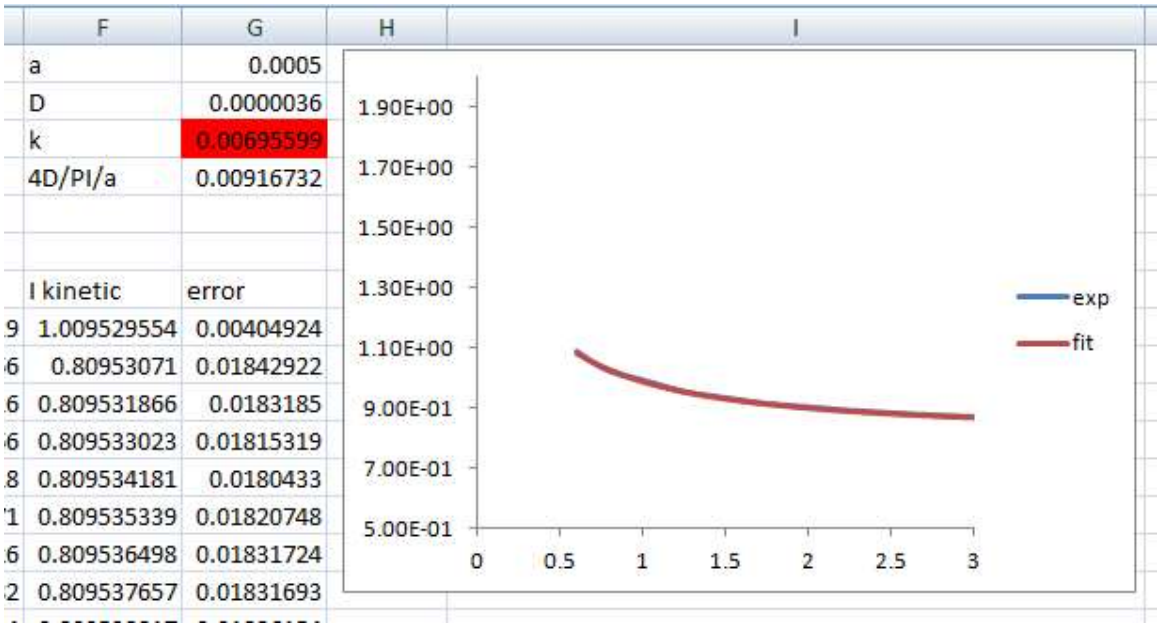

	F	G
	a	0.0005
	D	0.0000036
	k	0.00695599
	4D/PI/a	0.00916732
	I kinetic	error
9	1.009529554	0.00404924
6	0.80953071	0.01842922
6	0.809531866	0.0183185
6	0.809533023	0.01815319
8	0.809534181	0.0180433
1	0.809535339	0.01820748
6	0.809536498	0.01831724
2	0.809537657	0.01831693

PAC_Fit Method

Heterogeneous electron transfer rates can also be determined using the LabView program PAC_Fit. After opening the standalone version of PAC_Fit, the program will prompt to load data in the upper left hand corner. It will automatically parse a standard text file generated from a CHI SECM potentiostat.

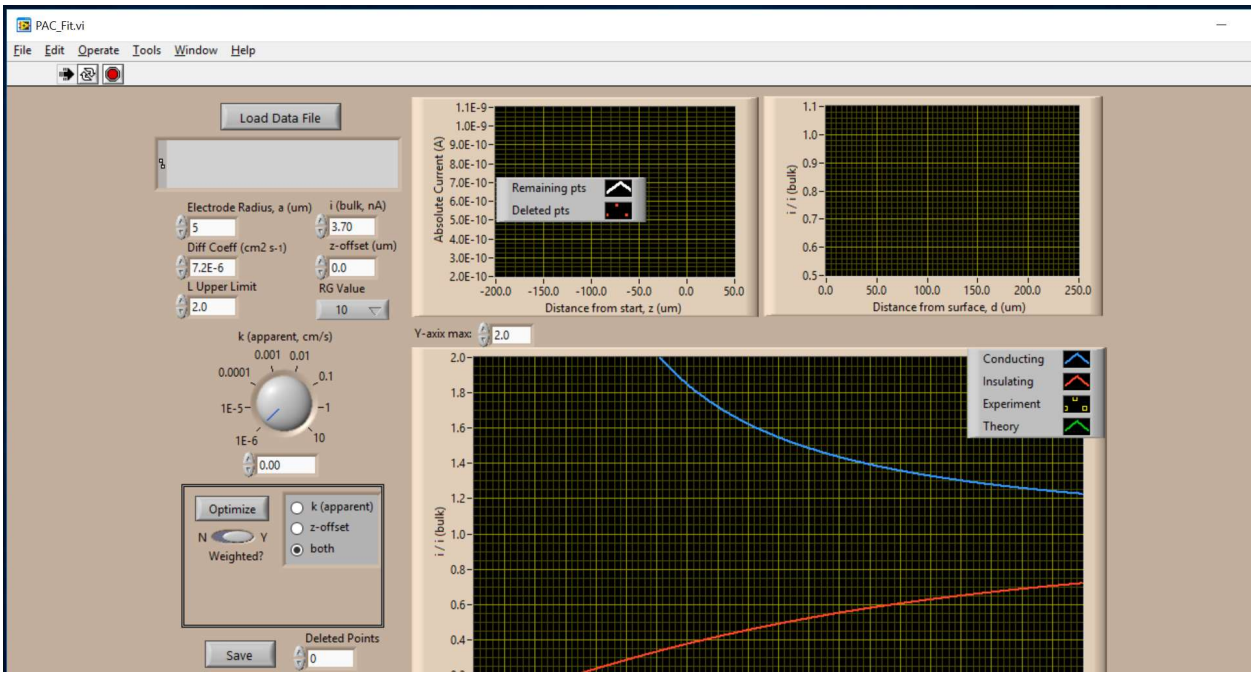

After loading the data, input a “i (bulk, nA)” value to bring the data in the range of the fit.

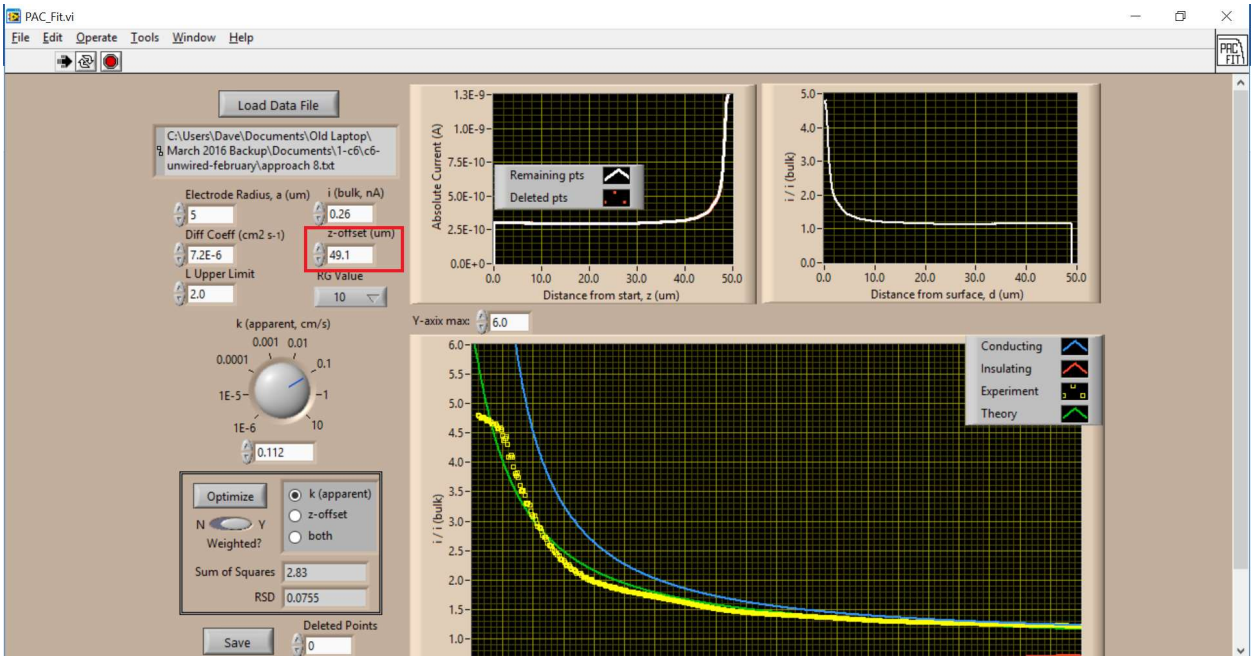

Adjust the z-offset until the approach curve makes contact. Delete extraneous points.

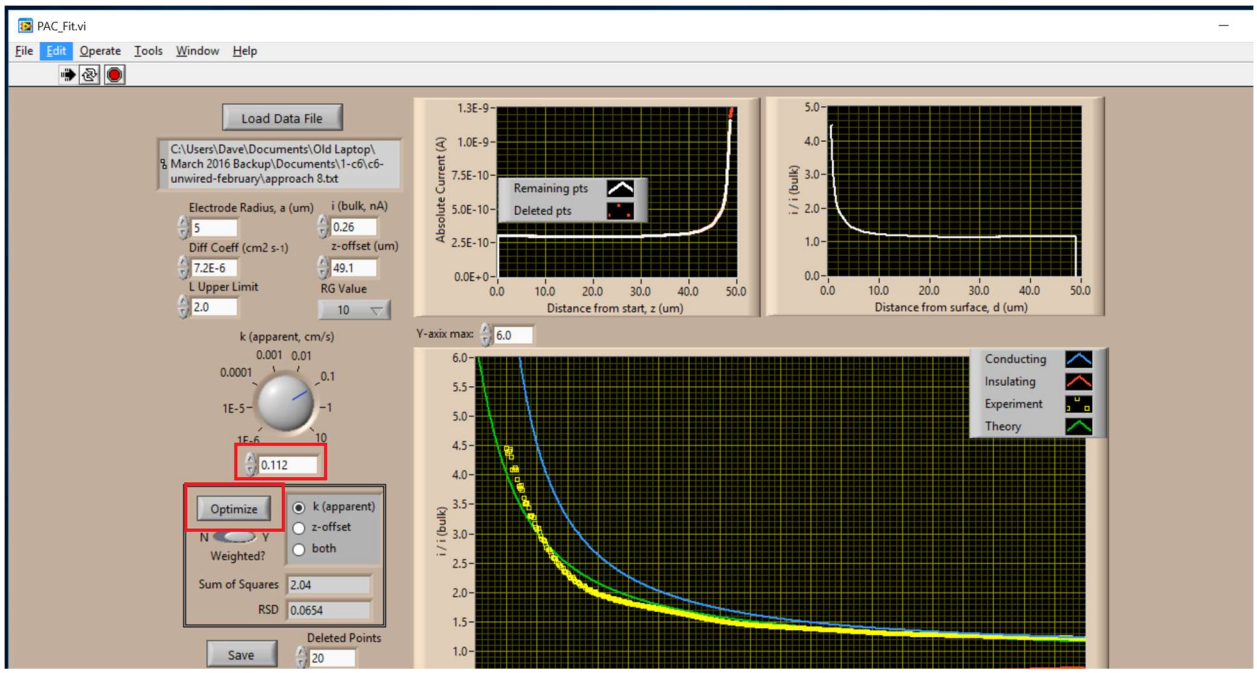

Click optimize and the value below the dial will be the k_f value. While this method is useful for analyzing negative feedback and large current systems, it is not precise enough to measure lower current outputs typical of some nanoparticle samples.

APPENDIX C

SYNTHESIS OF STILBENETHIOL

4-mercaptostilbene was synthesized using the procedure outlined by Cao et. al.[98]

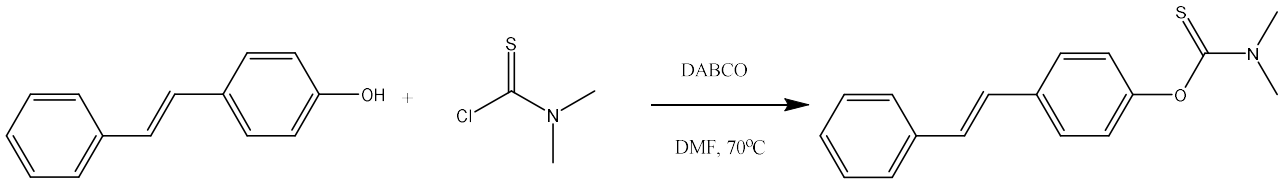

1

Compound 1 was synthesized according to Nowakowska.[99,100] 5 mmol of hydroxystilbene (1 g) was dissolved in 20 ml of dimethylformamide. 20 mmol of 1,4-diazabicyclo[2,2,2]octane (DABCO) (2.24 g) and 10 mmol of N,N-dimethylthiocarbamoyl chloride (1.23 g) were added to the solution and heated at 70ºC for 5 h. The mixture was poured into 0ºC water and acidified to pH 3 with concentrated hydrochloric acid. The precipitate was obtained using gravity filtration and washed with cold water. The product was then recrystallized in a mixture of ethanol and hexane (vol:vol, 95:5) to form pure compound 1.

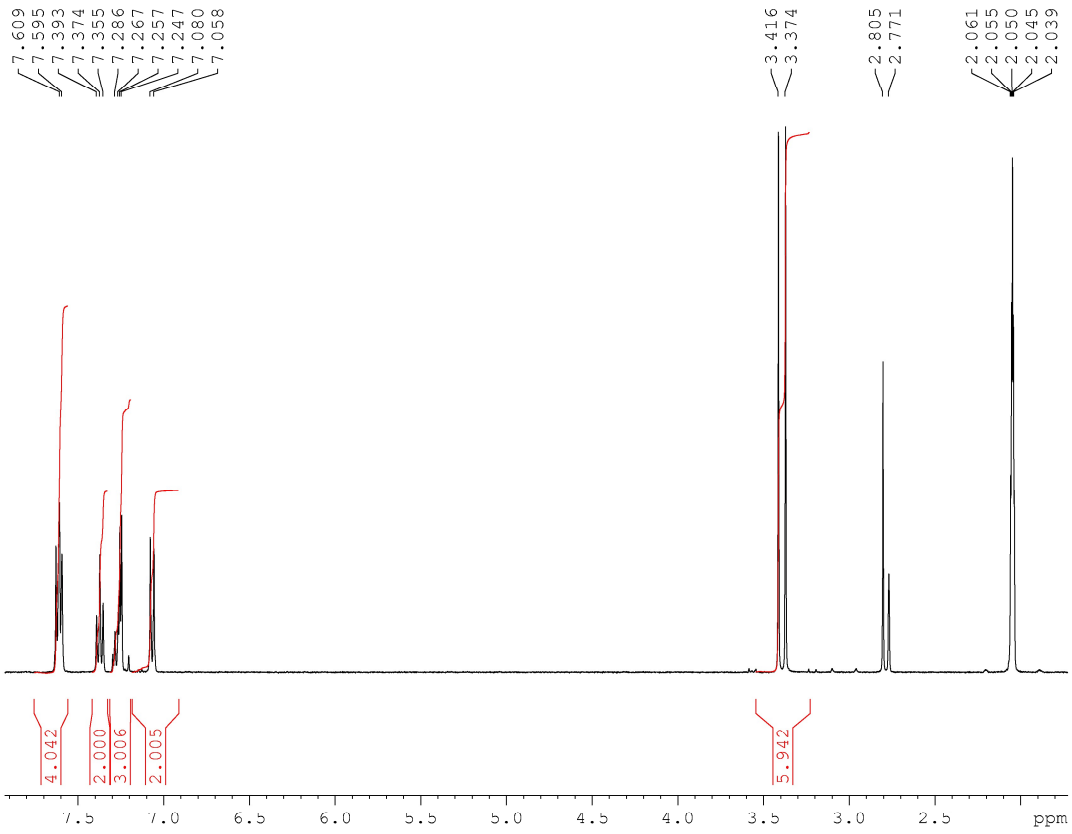

Figure B1. ^{1}H-NMR of Compound 1 in $(CD_3)_2CO$.

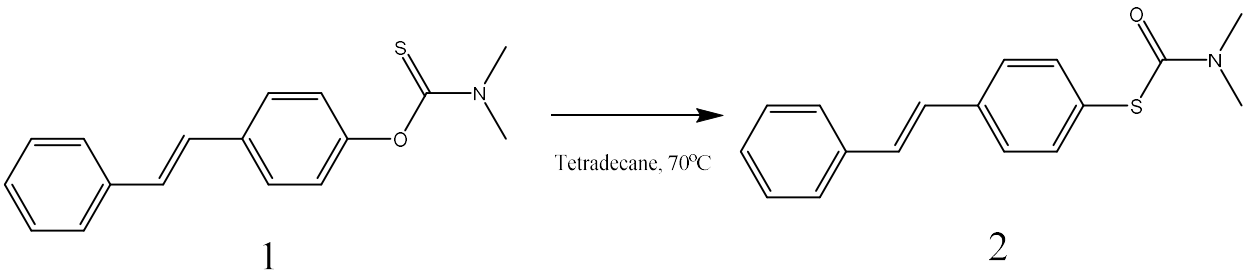

1 2

Compound 2 was synthesized according to a modified method.[101] Compound 1 was dissolved in 45 mL of tetradecane and heated to 220°C for 5 hours. After cooling the mixture overnight to room temperature, the solution was added to a silica column packed with mixture of

hexanes and ethyl acetate (vol:vol, 1:7). The column was washed with hexanes and the product was recrystallized from a mixture of ethanol and hexane (vol:vol, 95:5) to provide compound 2.

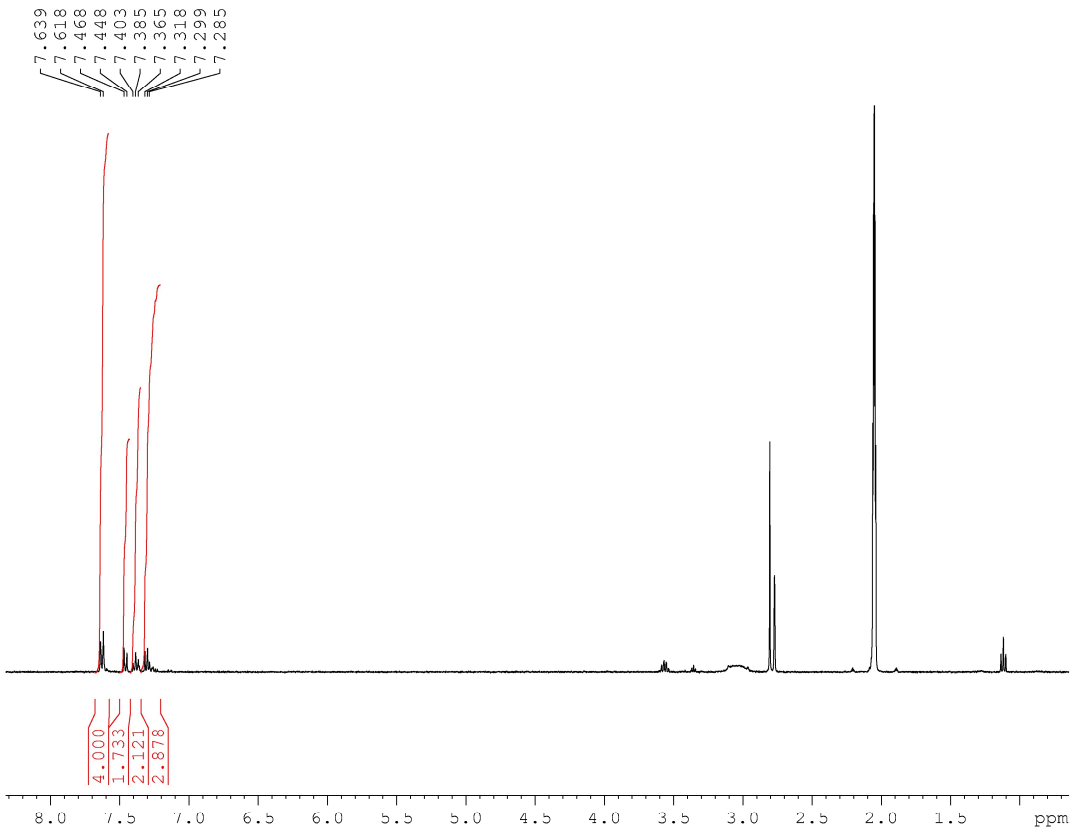

Figure B2. ^{1}H-NMR Compound 2 in $(CD_3)_2CO$.

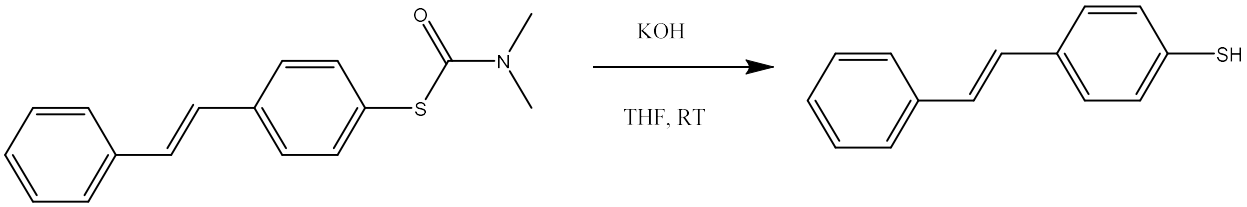

2

4-mercaptostilbene was finally synthesized using a previously published method.[100,101] In 25 mL of tetrahydrofurane, 2.5 molar equivalents of potassium hydroxide in methanol were added

to 1 molar equivalent of compound 2. The reaction mixture was stirred at room temperature overnight then poured into 0ºC water and acidified to pH 3 using 6.0 N hydrochloric acid. The product was collected by filtration and recrystallized from a mixture of ethanol and hexane (vol:vol, 1:1).

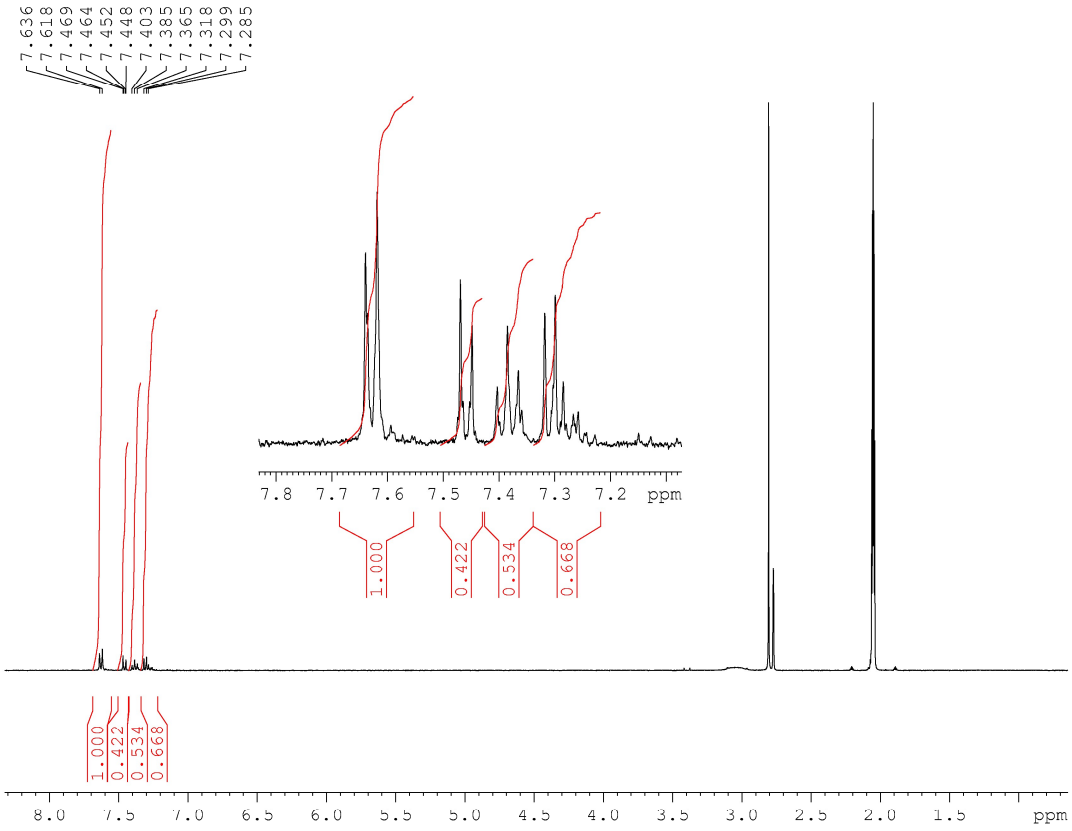

Figure B3. ^{1}H-NMR of stilbenethiol in $(CD_3)_2CO$.

^{1}H-NMR Peak Assignments

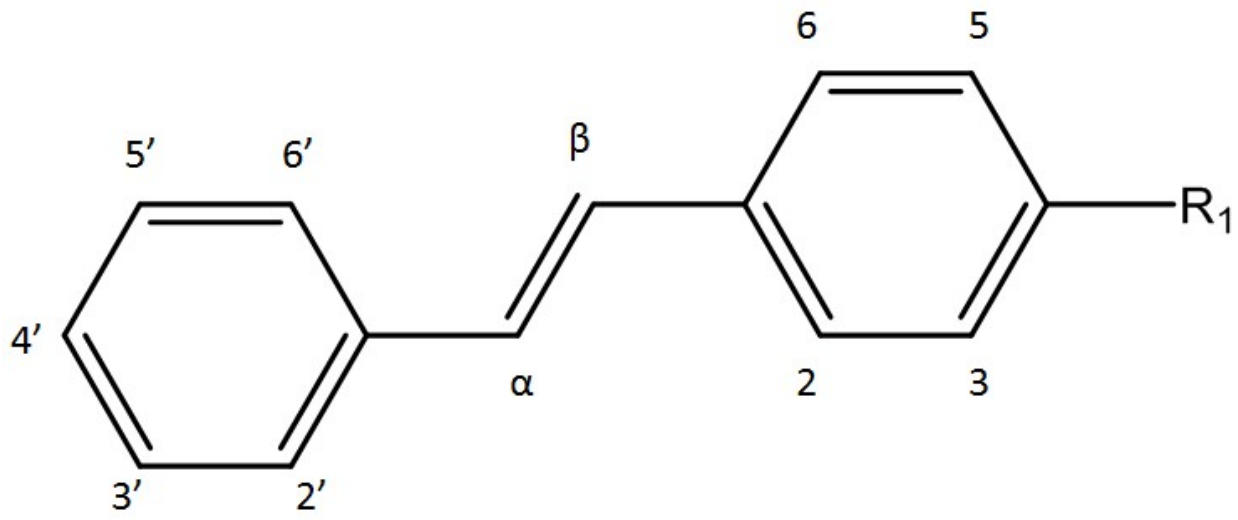

Figure B4. Labeled protons for the compounds synthesized where R_1 is O-C(S)-N$(CH_3)_2$ for Compound 1, S-C(O)-N$(CH_3)_2$ for Compound 2, and SH for stilbenethiol.

Table B1. Peak assignments

^{1}H	**1**	**2**	**Stilbenethiol**
α	7.26	7.30	7.28
β	7.26	7.30	7.28
2',6'	7.60	7.40	7.46
3',5'	7.40	7.37	7.36
2,6	7.59	7.62	7.61
3,5	7.07	7.30	7.31
N-$(CH_3)_2$	3.40	3.02	-

While the peaks present are in agreement with previous literature,[99] the integrations for Compound 2 and stilbenethiol are not in agreement with the structure. This is indicative that the synthesis did not go to completion and there is room for improvement during purification.

REFERENCES

(1) Kazmerski, L. L. Solar Photovoltaics R&D at the Tipping Point: A 2005 Technology Overview. *J. Electron Spectros. Relat. Phenomena* **2006**, *150*, 105–135.

(2) Hemminger, J.; Bare, S.; Berrah, N.; Ceyer, S.; Clark, S.; Cummings, P. *New Science for a Secure and Sustainable Energy Future: A Report From the Basic Energy Sciences Advisory Committee*; 2008.

(3) Lu, K. *Materials in Energy Conversion, Harvesting, and Storage*; Wiley, 2014.

(4) *Water Energy Nexus Full Report*; 2014.

(5) Maupin, M.; Kenny, J.; Hutson, S.; Lovelace, J.; Barber, N.; Linsey, K. *Estimated Use of Water in the United States in 2010*; 2014.

(6) Beam, J. C.; LeBlanc, G.; Gizzie, E. A.; Ivanov, B. L.; Needell, D. R.; Shearer, M. J.; Jennings, G. K.; Lukehart, C. M.; Cliffel, D. E. Construction of a Semiconductor-Biological Interface for Solar Energy Conversion: P-Doped Silicon/Photosystem I/Zinc Oxide. *Langmuir* **2015**, *31*, 10002–10007.

(7) Gizzie, E. A.; Scott Niezgoda, J.; Robinson, M. T.; Harris, A. G.; Kane Jennings, G.; Rosenthal, S. J.; Cliffel, D. E. Photosystem I-polyaniline/TiO 2 Solid-State Solar Cells: Simple Devices for Biohybrid Solar Energy Conversion. *Energy Environ. Sci.* **2015**, *8*, 3572–3576.

(8) Wuelfing, W. P.; Green, S. J.; Pietron, J. J.; Cliffel, D. E.; Murray, R. W. Electronic Conductivity of Solid-State, Mixed-Valent, Monolayer-Protected Au Clusters. *J. Am. Chem. Soc.* **2000**, *122*, 11465–11472.

(9) Wuelfing, W. P.; Murray, R. W. Electron Hopping through Films of Arenethiolate Monolayer-Protected Gold Clusters. *J. Phys. Chem. B* **2002**, *106*, 3139–3145.

(10) Antonello, S.; Holm, A. H.; Instuli, E.; Maran, F. Molecular Electron-Transfer Properties of Au38 Clusters. *J. Am. Chem. Soc.* **2007**, *129*, 9836–9837.

(11) Terrill, R. H.; Postlethwaite, T. A.; Chen, C.; Poon, C.-D.; Terzis, A.; Chen, A.; Hutchison, J. E.; Clark, M. R.; Wignall, G. Monolayers in Three Dimensions: NMR, SAXS, Thermal, and Electron Hopping Studies of Alkanethiol Stabilized Gold Clusters. *J. Am. Chem. Soc.* **1995**, *117*, 12537–12548.

(12) Brust, M.; Walker, M.; Bethell, D.; Schiffrin, D. J.; Whyman, R. Synthesis of Thiol-Derivatised Gold Nanoparticles in a Two-Phase Liquid-Liquid System. *J. Chem. Soc. Chem. Commun.* **1994**, 801–802.

(13) Green, S. J.; Stokes, J. J.; Hostetler, M. J.; Pietron, J.; Murray, R. W. Three-Dimensional Monolayers: Nanometer-Sized Electrodes of Alkanethiolate-Stabilized Gold Cluster Molecules. *J. Phys. Chem. B* **1997**, *101*, 2663–2668.

(14) Peterson, R. R.; Cliffel, D. E. Scanning Electrochemical Microscopy Determination of

Organic Soluble MPC Electron-Transfer Rates . *Langmuir* **2006**, *22*, 10307–10314.

(15) Templeton, A. C.; Chen, S.; Gross, S. M.; Murray, R. W. Water-Soluble, Isolable Gold Clusters Protected by Tiopronin and Coenzyme A Monolayers. *Langmuir* **1998**, *15*, 66–76.

(16) Jung, J.; Kang, S.; Han, Y.-K. Ligand Effects on the Stability of Thiol-Stabilized Gold Nanoclusters: Au25(SR)18(-), Au38(SR)24, and Au102(SR)44. *Nanoscale* **2012**, *4*, 4206–4210.

(17) Chen, S.; Murray, R. W.; Feldberg, S. W. Quantized Capacitance Charging of Monolayer-Protected Au Clusters. *J. Phys. Chem. B* **1998**, *102*, 9898–9907.

(18) Heaven, M. W.; Dass, A.; White, P. S.; Holt, K. M.; Murray, R. W. Crystal Structure of the Gold Nanoparticle [N(C8H17)4][Au25(SCH2CH2Ph)18]. *J. Am. Chem. Soc.* **2008**, *130*, 3754–3755.

(19) Hostetler, M. J.; Templeton, A. C.; Murray, R. W. Dynamics of Place-Exchange Reactions on Monolayer-Protected Gold Cluster Molecules. *Langmuir* **1999**, *15*, 3782–3789.

(20) Montalti, M.; Prodi, L.; Zaccheroni, N.; Baxter, R.; Teobaldi, G.; Zerbetto, F. Kinetics of Place-Exchange Reactions of Thiols on Gold Nanoparticles. *Langmuir* **2003**, *19*, 5172–5174.

(21) Venkateswaran, K.; Moser, D. P.; Dollhopf, M. E.; Lies, D. P.; Saffarini, D. A.; MacGregor, B. J.; Ringelberg, D. B.; White, D. C.; Nishijima, M.; Sano, H.; *et al.* Polyphasic Taxonomy of the Genus Shewanella and Description of Shewanella Oneidensis Sp. Nov. *Int. J. Syst. Bacteriol.* **1999**, *49 Pt 2*, 705–724.

(22) Myers, C. R.; Nealson, K. H. Bacterial Manganese Reduction and Growth with Manganese Oxide as the Sole Electron Acceptor. *Science* **1988**, *240*, 1319–1321.

(23) Stenström, I. M.; Molin, G. Classification of the Spoilage Flora of Fish, with Special Reference to Shewanella Putrefaciens. *J. Appl. Bacteriol.* **1990**, *68*, 601–618.

(24) Hau, H. H.; Gralnick, J. A. Ecology and Biotechnology of the Genus Shewanella. *Annu. Rev. Microbiol.* **2007**, *61*, 237–258.

(25) Logan, B. E.; Rabaey, K. Conversion of Wastes into Bioelectricity and Chemicals by Using Microbial Electrochemical Technologies. *Science* **2012**, *337*, 686–690.

(26) Lovley, D. R. Bioremediation of Organic and Metal Contaminants with Dissimilatory Metal Reduction. *J. Ind. Microbiol.* **1995**, *14*, 85–93.

(27) Elias, D. A.; Krumholz, L. R.; Wong, D.; Long, P. E.; Suflita, J. M. Characterization of Microbial Activities and U Reduction in a Shallow Aquifer Contaminated by Uranium Mill Tailings. *Microb. Ecol.* **2003**, *46*, 83–91.

(28) Myers, J. M.; Myers, C. R. Role for Outer Membrane Cytochromes OmcA and OmcB of

Shewanella Putrefaciens MR-1 in Reduction of Manganese Dioxide. *Appl. Environ. Microbiol.* **2001**, *67*, 260–269.

(29) Reguera, G.; McCarthy, K. D.; Mehta, T.; Nicoll, J. S.; Tuominen, M. T.; Lovley, D. R. Extracellular Electron Transfer via Microbial Nanowires. *Nature* **2005**, *435*, 1098–1101.

(30) Gorby, Y. A.; Yanina, S.; McLean, J. S.; Rosso, K. M.; Moyles, D.; Dohnalkova, A.; Beveridge, T. J.; Chang, I. S.; Kim, B. H.; Kim, K. S.; *et al.* Electrically Conductive Bacterial Nanowires Produced by Shewanella Oneidensis Strain MR-1 and Other Microorganisms. *Proc. Natl. Acad. Sci. U. S. A.* **2006**, *103*, 11358–11363.

(31) Marsili, E.; Baron, D. B.; Shikhare, I. D.; Coursolle, D.; Gralnick, J. A.; Bond, D. R. Shewanella Secretes Flavins That Mediate Extracellular Electron Transfer. *Proc. Natl. Acad. Sci. U. S. A.* **2008**, *105*, 3968–3973.

(32) von Canstein, H.; Ogawa, J.; Shimizu, S.; Lloyd, J. R. Secretion of Flavins by Shewanella Species and Their Role in Extracellular Electron Transfer. *Appl. Environ. Microbiol.* **2008**, *74*, 615–623.

(33) Jiang, X.; Hu, J.; Fitzgerald, L. A.; Biffinger, J. C.; Xie, P.; Ringeisen, B. R.; Lieber, C. M. Probing Electron Transfer Mechanisms in Shewanella Oneidensis MR-1 Using a Nanoelectrode Platform and Single-Cell Imaging. *Proc. Natl. Acad. Sci. U. S. A.* **2010**, *107*, 16806–16810.

(34) Bard, A. J.; Mirkin, M. V. *Scanning Electrochemical Microscopy*; 2nd ed.; CRC Press LLC, 2012.

(35) Bard, A. J.; Faulkner, L. R. *Electrochemical Methods: Fundamentals and Applications*; 2nd ed.; 2001.

(36) Bard, A. J.; Rubinstein, I. *Electroanalytical Chemistry: A Series of Advances*; Taylor & Francis, 2003.

(37) Amemiya, S.; Ding, Z.; Zhou, J.; Bard, A. J. Studies of Charge Transfer at Liquid | Liquid Interfaces and Bilayer Lipid Membranes by Scanning Electrochemical Microscopy. *J. Electroanal. Chem.* **2000**, *483*, 7–17.

(38) Bard, A. J.; Fan, F. R. F.; Kwak, J.; Lev, O. Scanning Electrochemical Microscopy. Introduction and Principles. *Anal. Chem.* **1989**, *61*, 132–138.

(39) Pletcher, D.; Group, S. E. *Instrumental Methods in Electrochemistry*; HorwoodPublishing, 2001.

(40) Wittstock, G.; Burchardt, M.; Pust, S. E.; Shen, Y.; Zhao, C. Scanning Electrochemical Microscopy for Direct Imaging of Reaction Rates. *Angew. Chem. Int. Ed. Engl.* **2007**, *46*, 1584–1617.

(41) Slevin, C. J.; Liljeroth, P.; Kontturi, K. Measurement of the Adsorption of Drug Ions at Model Membranes by Scanning Electrochemical Microscopy. *Langmuir* **2003**, *19*, 2851–2858.

(42) Gyurcsányi, R. E.; Pergel, É.; Nagy, R.; Kapui, I.; Thu Lan, B. T.; Tóth, K.; Bitter, I.; Lindner, E. Direct Evidence of Ionic Fluxes Across Ion-Selective Membranes: A Scanning Electrochemical Microscopic and Potentiometric Study. *Anal. Chem.* **2001**, *73*, 2104–2111.

(43) Bertoncello, P.; Ciani, I.; Li, F.; Unwin, P. R. Measurement of Apparent Diffusion Coefficients within Ultrathin Nafion Langmuir-Schaefer Films: Comparison of a Novel Scanning Electrochemical Microscopy Approach with Cyclic Voltammetry. *Langmuir* **2006**, *22*, 10380–10388.

(44) Williams, M. E.; Stevenson, K. J.; Massari, A. M.; Hupp, J. T. Imaging Size-Selective Permeation through Micropatterned Thin Films Using Scanning Electrochemical Microscopy. *Anal. Chem.* **2000**, *72*, 3122–3128.

(45) Abucayon, E.; Ke, N.; Cornut, R.; Patelunas, A.; Miller, D.; Nishiguchi, M. K.; Zoski, C. G. Investigating Catalase Activity through Hydrogen Peroxide Decomposition by Bacteria Biofilms in Real Time Using Scanning Electrochemical Microscopy. *Anal. Chem.* **2014**, *86*, 498–505.

(46) Beaulieu, I.; Kuss, S.; Mauzeroll, J.; Geissler, M. Biological Scanning Electrochemical Microscopy and Its Application to Live Cell Studies. *Anal. Chem.* **2011**, *83*, 1485–1492.

(47) Koley, D.; Ramsey, M. M.; Bard, A. J.; Whiteley, M. Discovery of a Biofilm Electrocline Using Real-Time 3D Metabolite Analysis. *Proc. Natl. Acad. Sci. 108*, 19996–20001.

(48) Barfidokht, A.; Ciampi, S.; Luais, E.; Darwish, N.; Gooding, J. J. Distance-Dependent Electron Transfer at Passivated Electrodes Decorated by Gold Nanoparticles. *Anal. Chem.* **2013**, *85*, 1073–1080.

(49) Chazalviel, J.-N.; Allongue, P. On the Origin of the Efficient Nanoparticle Mediated Electron Transfer across a Self-Assembled Monolayer. *J. Am. Chem. Soc.* **2011**, *133*, 762–764.

(50) Hicks, J. F.; Templeton, A. C.; Chen, S. W.; Sheran, K. M.; Jasti, R.; Murray, R. W.; Debord, J.; Schaaff, G.; Whetton, R. L. The Monolayer Thickness Dependence of Quantized Double Layer Capacitances of Monolayer Protected Gold Clusters. *Anal. Chem.* **1999**, *71*, 3703–3711.

(51) Murray, R. W. Nanoelectrochemistry: Metal Nanoparticles, Nanoelectrodes, and Nanopores. *Chem. Rev.* **2008**, *108*, 2688–2720.

(52) Ung, T.; Giersig, M.; Dunstan, D.; Mulvaney, P. Spectroelectrochemistry of Colloidal Silver. *Langmuir* **1997**, *13*, 1773–1782.

(53) Nitzan, A.; Ratner, M. A. Electron Transport in Molecular Wire Junctions. *Science (80-.).* **2003**, *300*, 1384–1389.

(54) Karzazi, Y.; Cornil, J.; BrÃ©das, J. L. Resonant Tunnelling Diodes Based on Molecular Wires Incorporating Saturated Spacers: A Quantum-Chemical Study. *Nanotechnology* **2002**, *13*, 336.

(55) Berlin, Y. A.; Hutchison, G. R.; Rempala, P.; Ratner, M. A.; Michl, J. Charge Hopping in Molecular Wires as a Sequence of Electron-Transfer Reactions. *J. Phys. Chem. A* **2003**, *107*, 3970–3980.

(56) Tour, J. M.; Rawlett, A. M.; Kozaki, M.; Yao, Y.; Jagessar, R. C.; Dirk, S. M.; Price, D. W.; Reed, M. A.; Zhou, C.-W.; Chen, J.; *et al.* Synthesis and Preliminary Testing of Molecular Wires and Devices. *Chem. - A Eur. J.* **2001**, *7*, 5118–5134.

(57) Schubert, C.; Margraf, J. T.; Clark, T.; Guldi, D. M. Molecular Wires--Impact of π-Conjugation and Implementation of Molecular Bottlenecks. *Chem. Soc. Rev.* **2015**, *44*, 988–998.

(58) Leary, E.; La Rosa, A.; González, M. T.; Rubio-Bollinger, G.; Agraït, N.; Martín, N. Incorporating Single Molecules into Electrical Circuits. The Role of the Chemical Anchoring Group. *Chem. Soc. Rev.* **2015**, *44*, 920–942.

(59) Guldi, D. M.; Nishihara, H.; Venkataraman, L. Molecular Wires. *Chem. Soc. Rev.* **2015**, *44*, 842–844.

(60) Sukegawa, J.; Schubert, C.; Zhu, X.; Tsuji, H.; Guldi, D. M.; Nakamura, E. Electron Transfer through Rigid Organic Molecular Wires Enhanced by Electronic and Electron-Vibration Coupling. *Nat. Chem.* **2014**, *6*, 899–905.

(61) Cygan, M. T.; Dunbar, T. D.; Arnold, J. J.; Bumm, L. A.; Shedlock, N. F.; Burgin, T. P.; Jones, L.; Allara, D. L.; Tour, J. M.; Weiss, P. S. Insertion, Conductivity, and Structures of Conjugated Organic Oligomers in Self-Assembled Alkanethiol Monolayers on Au{111}. *J. Am. Chem. Soc.* **1998**, *120*, 2721–2732.

(62) Bumm, L. A.; Arnold, J. J.; Cygan, M. T.; Dunbar, T. D.; Burgin, T. P.; Jones, L.; Allara, D. L.; Tour, J. M.; Weiss, P. S. Are Single Molecular Wires Conducting? *Science (80-.).* **1996**, *271*, 1705–1707.

(63) Kushmerick, J. J.; Pollack, S. K.; Yang, J. C.; Naciri, J.; Holt, D. B.; Ratner, M. A.; Shashidhar, R. Understanding Charge Transport in Molecular Electronics. *Ann. N. Y. Acad. Sci.* **2003**, *1006*, 277–290.

(64) Feldheim, D. L.; Foss, C. A. *Metal Nanoparticles: Synthesis, Characterization, and Applications*; CRC Press LLC, 2002.

(65) Gerdon, A. E.; Wright, D. W.; Cliffel, D. E. Hemagglutinin Linear Epitope Presentation on Monolayer-Protected Clusters Elicits Strong Antibody Binding. *Biomacromolecules* **2005**, *6*, 3419–3424.

(66) Gerdon, A. E.; Wright, D. W.; Cliffel, D. E. Epitope Mapping of the Protective Antigen of B. Anthracis by Using Nanoclusters Presenting Conformational Peptide Epitopes. *Angew. Chemie Int. Ed.* **2006**, *45*, 594–598.

(67) Hicks, J. F.; Miles, D. T.; Murray, R. W. Quantized Double-Layer Charging of Highly Monodisperse Metal Nanoparticles. *J. Am. Chem. Soc.* **2002**, *124*, 13322–13328.

(68) Hicks, J. F.; Zamborini, F. P.; Murray, R. W. Dynamics of Electron Transfers between Electrodes and Monolayers of Nanoparticles. *J. Phys. Chem. B* **2002**, *106*, 7751–7757.

(69) Schaaff, T. G.; Knight, G.; Shafigullin, M. N.; Borkman, R. F.; Whetten, R. L. Isolation and Selected Properties of a 10.4 kDa Gold:Glutathione Cluster Compound. *J. Phys. Chem. B* **1998**, *102*, 10643–10646.

(70) Xu, R.; Sun, Y.; Yang, J.-Y.; He, L.; Nie, J.-C.; Li, L.; Li, Y. Inhibited Single-Electron Transfer by Electronic Band Gap of Two-Dimensional Au Quantum Dot Superlattice. *Appl. Phys. Lett.* **2010**, *97*, 113101.

(71) Liu, X.; Niu, W.; Li, H.; Han, S.; Hu, L.; Xu, G. Glucose Biosensor Based on Gold Nanoparticle-Catalyzed Luminol Electrochemiluminescence on a Three-Dimensional Sol–gel Network. *Electrochem. commun.* **2008**, *10*, 1250–1253.

(72) Jain, P. K.; Huang, X.; El-Sayed, I. H.; El-Sayed, M. A. Noble Metals on the Nanoscale: Optical and Photothermal Properties and Some Applications in Imaging, Sensing, Biology, and Medicine. *Acc. Chem. Res.* **2008**, *41*, 1578–1586.

(73) Daniel, M.-C.; Astruc, D. Gold Nanoparticles: Assembly, Supramolecular Chemistry, Quantum-Size-Related Properties, and Applications toward Biology, Catalysis, and Nanotechnology. *Chem. Rev.* **2004**, *104*, 293–346.

(74) Qiao, Y.; Chen, H.; Lin, Y.; Huang, J. Controllable Synthesis of Water-Soluble Gold Nanoparticles and Their Applications in Electrocatalysis and Surface-Enhanced Raman Scattering. *Langmuir* **2011**, *27*, 11090–11097.

(75) Shah, M.; Badwaik, V. D.; Dakshinamurthy, R. Biological Applications of Gold Nanoparticles. *J. Nanosci. Nanotechnol.* **2014**, *14*, 344–362.

(76) Heuer-Jungemann, A.; Harimech, P. K.; Brown, T.; Kanaras, A. G. Gold Nanoparticles and Fluorescently-Labelled DNA as a Platform for Biological Sensing. *Nanoscale* **2013**, *5*, 9503–9510.

(77) Alvarez-Puebla, R. A.; Agarwal, A.; Manna, P.; Khanal, B. P.; Aldeanueva-Potel, P.; Carbó-Argibay, E.; Pazos-Pérez, N.; Vigderman, L.; Zubarev, E. R.; Kotov, N. A.; *et al.* Gold Nanorods 3D-Supercrystals as Surface Enhanced Raman Scattering Spectroscopy Substrates for the Rapid Detection of Scrambled Prions. *Proc. Natl. Acad. Sci. U. S. A.* **2011**, *108*, 8157–8161.

(78) Delcea, M.; Sternberg, N.; Yashchenok, A. M.; Georgieva, R.; Bäumler, H.; Möhwald, H.; Skirtach, A. G. Nanoplasmonics for Dual-Molecule Release through Nanopores in the Membrane of Red Blood Cells. *ACS Nano* **2012**, *6*, 4169–4180.

(79) Crisostomo, D.; Greene, R. R.; Cliffel, D. E. Effect of Ligand Charge on Electron-Transfer Rates of Water-Soluble Gold Nanoparticles. *J. Phys. Chem. C* **2015**, *119*, 11296–11300.

(80) Peterson, R. R.; Cliffel, D. E. Continuous Free-Flow Electrophoresis of Water-Soluble Monolayer-Protected Clusters. *Anal. Chem.* **2005**, *77*, 4348–4353.

(81) Jensen, M. B.; Tallman, D. E. A LabVIEW-Based Virtual Instrument for Simulation and Analysis of SECM Approach Curves. *J. Solid State Electrochem.* **2013**, *17*, 2999–3003.

(82) McConnell, W. P.; Novak, J. P.; Brousseau, L. C.; Fuierer, R. R.; Tenent, R. C.; Feldheim, D. L. Electronic and Optical Properties of Chemically Modified Metal Nanoparticles and Molecularly Bridged Nanoparticle Arrays. *J. Phys. Chem. B* **2000**, *104*, 8925–8930.

(83) Brauer, G. *Handbook of Preparative Inoragnic Chemistry*; 2nd ed.; 1963.

(84) Lovley, D. R. The Microbe Electric: Conversion of Organic Matter to Electricity. *Curr. Opin. Biotechnol.* **2008**, *19*, 564–571.

(85) Rabaey, K.; Rozendal, R. A. Microbial Electrosynthesis - Revisiting the Electrical Route for Microbial Production. *Nat. Rev. Microbiol.* **2010**, *8*, 706–716.

(86) Ross, D. E.; Flynn, J. M.; Baron, D. B.; Gralnick, J. A.; Bond, D. R. Towards Electrosynthesis in Shewanella: Energetics of Reversing the Mtr Pathway for Reductive Metabolism. *PLoS One* **2011**, *6*, e16649.

(87) Brutinel, E. D.; Gralnick, J. A. Shuttling Happens: Soluble Flavin Mediators of Extracellular Electron Transfer in Shewanella. *Appl. Microbiol. Biotechnol.* **2012**, *93*, 41–48.

(88) Gralnick, J. A.; Newman, D. K. Extracellular Respiration. *Mol. Microbiol.* **2007**, *65*, 1–11.

(89) Hernandez, M. E.; Newman, D. K. Extracellular Electron Transfer. *Cell. Mol. Life Sci.* **2001**, *58*, 1562–1571.

(90) Coursolle, D.; Baron, D. B.; Bond, D. R.; Gralnick, J. A. The Mtr Respiratory Pathway Is Essential for Reducing Flavins and Electrodes in Shewanella Oneidensis. *J. Bacteriol.* **2010**, *192*, 467–474.

(91) Baron, D.; LaBelle, E.; Coursolle, D.; Gralnick, J. A.; Bond, D. R. Electrochemical Measurement of Electron Transfer Kinetics by Shewanella Oneidensis MR-1. *J. Biol. Chem.* **2009**, *284*, 28865–28873.

(92) Nevin, K. P.; Lovley, D. R. Mechanisms for Accessing Insoluble Fe(III) Oxide during Dissimilatory Fe(III) Reduction by Geothrix Fermentans. *Appl. Environ. Microbiol.* **2002**, *68*, 2294–2299.

(93) Lies, D. P.; Hernandez, M. E.; Kappler, A.; Mielke, R. E.; Gralnick, J. A.; Newman, D. K. Shewanella Oneidensis MR-1 Uses Overlapping Pathways for Iron Reduction at a Distance and by Direct Contact under Conditions Relevant for Biofilms. *Appl. Environ. Microbiol.* **2005**, *71*, 4414–4426.

(94) Chen, G. Electrochemical Analysis and Scanning Electrochemical Microscopy Investigations of Photosystem I, Vanderbilt University, 2013.

(95) Marsili, E.; Rollefson, J. B.; Baron, D. B.; Hozalski, R. M.; Bond, D. R. Microbial Biofilm Voltammetry: Direct Electrochemical Characterization of Catalytic Electrode-

Attached Biofilms. *Appl. Environ. Microbiol.* **2008**, *74*, 7329–7337.

(96) Harkness, K. M.; Hixson, B. C.; Fenn, L. S.; Turner, B. N.; Rape, A. C.; Simpson, C. A.; Huffman, B. J.; Okoli, T. C.; McLean, J. A.; Cliffel, D. E. A Structural Mass Spectrometry Strategy for the Relative Quantitation of Ligands on Mixed Monolayer-Protected Gold Nanoparticles. *Anal. Chem.* **2010**, *82*, 9268–9274.

(97) Zhang, W.; Wu, H.; Hsing, I.-M. Real-Time Label-Free Monitoring of Shewanella Oneidensis MR-1 Biofilm Formation on Electrode During Bacterial Electrogenesis Using Scanning Electrochemical Microscopy. *Electroanalysis* **2015**, *27*, 648–655.

(98) Cao, X.-Y.; Yang, J.; Dai, F.; Ding, D.-J.; Kang, Y.-F.; Wang, F.; Li, X.-Z.; Liu, G.-Y.; Yu, S.-S.; Jin, X.-L.; *et al.* Extraordinary Radical Scavengers: 4-Mercaptostilbenes. *Chemistry* **2012**, *18*, 5898–5905.

(99) Nowakowska, Z. Structural Assignment of Stilbenethiols and Chalconethiols and Differentiation of Their Isomeric Derivatives by Means of 1 H- and 13 C-NMR Spectroscopy. *Spectrosc. Lett.* **2005**, *38*, 477–485.

(100) Nowakowska, Z. The Conversion of Stilbenols to Stilbenethiols via N,N-Dimethylthiocarbamates. *Phosphorus. Sulfur. Silicon Relat. Elem.* **2006**, *181*, 707–715.

(101) Mizuno, C. S.; Schrader, K. K.; Rimando, A. M. Algicidal Activity of Stilbene Analogues. *J. Agric. Food Chem.* **2008**, *56*, 9140–9145.